Pancreatic Adenocarcinoma Therapeutic Targets Revealed by Tumor-Stroma Cross-Talk Analyses in Patient-Derived Xenografts

Remy Nicolle, Yuna Blum, Laëtitia Marisa, Céline Loncle, Odile Gayet, Vincent Moutardier, Olivier Turrini, Marc Giovannini, Benjamin Bian, Martin Bigonnet, et al.

Article

Cell Reports

Pancreatic Adenocarcinoma Therapeutic Targets Revealed by Tumor-Stroma Cross-Talk Analyses in Patient-Derived Xenografts

Graphical Abstract

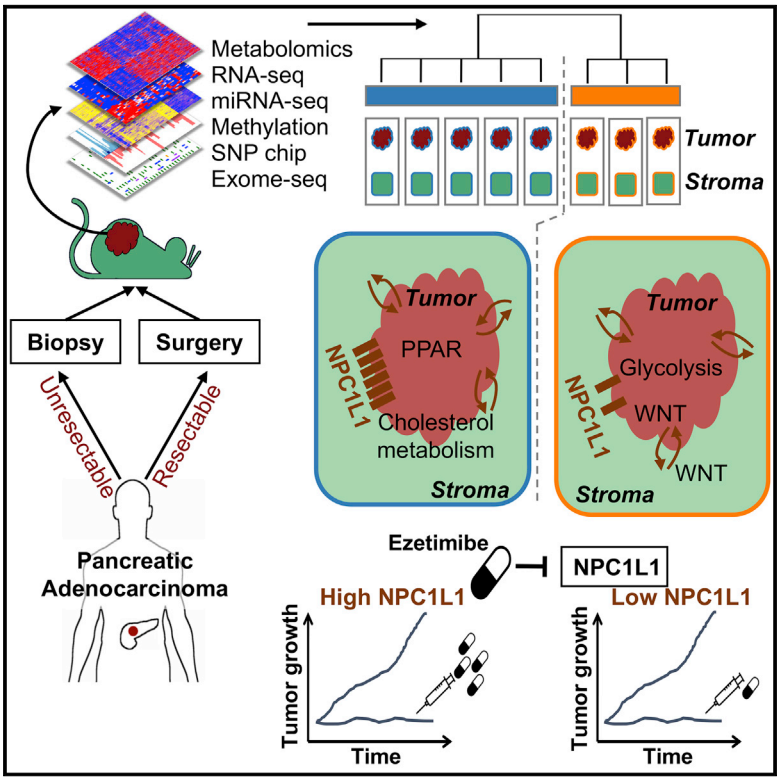

Highlights

- Patient xenografts are relevant models of pancreatic cancers and of their stroma
- Xenografts allow the genomic analysis of unresectable pancreatic cancers
- The epigenome, transcriptome, and stroma of pancreatic cancer define two subtypes
- Pancreatic cancer is sensitive to inhibition of *NPC1L1* by Ezetimibe

Authors

Rémy Nicolle, Yuna Blum, Laetitia Marisa, ..., Aurélien de Reyniès, Nelson Dusetti, Juan Iovanna

Correspondence

remy.nicolle@ligue-cancer.net (R.N.), juan.iovanna@inserm.fr (J.I.)

In Brief

Nicolle et al. present a genomic analysis of pancreatic cancer xenografts showing that tumor subtypes are defined by specific epigenetic, transcriptional, and stromal landscapes. They reveal potential therapeutic targets through analysis of signaling cross-talk between tumor and stromal cells.

Nicolle et al., 2017, Cell Reports *21*, 2458–2470
November 28, 2017
https://doi.org/10.1016/j.celrep.2017.11.003

OPEN ACCESS
CellPress

Cell Reports
Article

Pancreatic Adenocarcinoma Therapeutic Targets Revealed by Tumor-Stroma Cross-Talk Analyses in Patient-Derived Xenografts

Rémy Nicolle,[1,10,11,*] Yuna Blum,[1,10] Laetitia Marisa,[1,10] Celine Loncle,[2] Odile Gayet,[2] Vincent Moutardier,[3,4] Olivier Turrini,[4,5] Marc Giovannini,[5] Benjamin Bian,[2] Martin Bigonnet,[2] Marion Rubis,[2] Nabila Elarouci,[1] Lucile Armenoult,[1] Mira Ayadi,[1] Pauline Duconseil,[2] Mohamed Gasmi,[3] Mehdi Ouaissi,[5] Aurélie Maignan,[2] Gwen Lomberk,[7] Jean-Marie Boher,[5] Jacques Ewald,[5] Erwan Bories,[5] Jonathan Garnier,[2] Anthony Goncalves,[4,5] Flora Poizat,[5] Jean-Luc Raoul,[4,5] Veronique Secq,[3] Stephane Garcia,[3,4] Philippe Grandval,[4,6] Marine Barraud-Blanc,[6] Emmanuelle Norguet,[6] Marine Gilabert,[5] Jean-Robert Delpero,[4,5] Julie Roques,[2] Ezequiel Calvo,[8] Fabienne Guillaumond,[2] Sophie Vasseur,[2] Raul Urrutia,[9] Aurélien de Reyniès,[1] Nelson Dusetti,[2] and Juan Iovanna[2,*]

[1]Programme Cartes d'Identité des Tumeurs (CIT), Ligue Nationale Contre le Cancer, Paris, France
[2]Centre de Recherche en Cancérologie de Marseille (CRCM), INSERM U1068, CNRS UMR 7258, Institut Paoli-Calmettes, Aix Marseille Université, Marseille, France
[3]Hôpital Nord, Marseille, France
[4]Aix Marseille Université, Marseille, France
[5]Institut Paoli-Calmettes, Marseille, France
[6]Hôpital de la Timone, Marseille, France
[7]Division of Research, Department of Surgery, Medical College of Wisconsin, Milwaukee, WI 53226, USA
[8]Centre Génomique du Centre de Recherche du CHUL Research Center, Ville de Québec, QC, Canada
[9]Division of Research, Department of Surgery, Genomic Sciences and Precision Medicine Center, Medical College of Wisconsin, Milwaukee, WI 53226, USA
[10]These authors contributed equally
[11]Lead Contact
*Correspondence: remy.nicolle@ligue-cancer.net (R.N.), juan.iovanna@inserm.fr (J.I.)
https://doi.org/10.1016/j.celrep.2017.11.003

SUMMARY

Preclinical models based on patient-derived xenografts have remarkable specificity in distinguishing transformed human tumor cells from non-transformed murine stromal cells computationally. We obtained 29 pancreatic ductal adenocarcinoma (PDAC) xenografts from either resectable or non-resectable patients (surgery and endoscopic ultrasound-guided fine-needle aspirate, respectively). Extensive multiomic profiling revealed two subtypes with distinct clinical outcomes. These subtypes uncovered specific alterations in DNA methylation and transcription as well as in signaling pathways involved in tumor-stromal cross-talk. The analysis of these pathways indicates therapeutic opportunities for targeting both compartments and their interactions. In particular, we show that inhibiting NPC1L1 with Ezetimibe, a clinically available drug, might be an efficient approach for treating pancreatic cancers. These findings uncover the complex and diverse interplay between PDAC tumors and the stroma and demonstrate the pivotal role of xenografts for drug discovery and relevance to PDAC.

INTRODUCTION

Stratifying tumors using genome-wide molecular profiles has proven to be valuable for predicting therapeutic responses and clinical outcome in many neoplastic diseases. While pancreatic ductal adenocarcinoma (PDAC) is the fourth leading cause of cancer-related deaths, few integrative genomic, epigenomic, and transcriptomic studies have been conducted (Bailey et al., 2016; Cancer Genome Atlas Research Network [TCGA], 2017). This is mainly due to difficulty in obtaining an appropriate series of PDAC tumor samples. A major obstacle is the requirement for surgical samples resulting in the exclusion of the 85% non-resectable patients. Another critical issue is the high proportion of non-transformed stromal cells infiltrating the tumor, which greatly hinders the analysis of carcinogenic-specific processes. Despite these difficulties, the diversity of PDAC has been investigated recently using genome-wide approaches on surgical samples. A canonical study combining elegant laser capture microdissection followed by transcriptomic analysis revealed three main groups of patients: classical, quasi-mesenchymal, and exocrine-like (Collisson et al., 2011). The defined subtypes were suggested to differ in their clinical outcome and therapeutic responses. Another interesting study designed for tumor stratification and drug sensitivity reproduced this classification on a small number of samples (Noll et al., 2016). Moffitt and colleagues (Moffitt et al., 2015) involved a sophisticated computational approach using transcriptomic data and isolated cancerous, stromal, and normal tissue gene expression profiles. Analysis of estimated cancer-specific profiles identified two main tumor subtypes, including a basal-like subtype with a poor clinical outcome that bears great similarity to the basal-like tumors described in bladder and breast cancers. This study suggested that the exocrine-like subtype is attributable to the presence of normal non-transformed pancreatic

endocrine/exocrine epithelium. More recently, the Australian pancreatic cancer ICGC (International Cancer Genome Consortium) project defined four subtypes of PDAC based on the transcriptomic analysis of 96 selected primary tumors (Bailey et al., 2016), which they named squamous, pancreatic progenitor, immunogenic, and aberrantly differentiated endocrine exocrine (ADEX). Overall, solely based on gene expression, these studies recurrently found one specific subtype associated with a poor prognosis and a loss of differentiation that was either termed quasi-mesenchymal, basal-like, or squamous. However, no consensus arose from the subdivision of the well-differentiated PDAC tumors, particularly as none of the non-basal subtypes that were proposed are distinguishable based on their clinical outcome. In addition to the lack of non-resectable tumors, only one study proposed a model of the function and diversity of PDAC stroma (Bailey et al., 2016; Moffitt et al., 2015). Indeed, while the extensive desmoplasia present in PDAC tumors has raised major interrogations of its clinical impact and, more generally, on its function in the carcinogenic process (Carapuça et al., 2016; Rhim et al., 2014; Sherman et al., 2014; Tape et al., 2016), large-scale studies of the pancreatic tumor microenvironment are lacking.

Patient-derived xenografts (PDXs) are progressively appearing as a prime approach for much-needed preclinical studies and, in particular, to characterize drug efficacy by simulating phase II clinical trials (Gao et al., 2015; Townsend et al., 2016). PDXs have major advantages over cell lines as models of primary cancers. For instance, tumor cells preserve their complex 3D organization by being embedded in an active microenvironment with an elaborate and dynamic cellular composition. Importantly, xenografts of human primary PDAC enable "*ex patient*," but *in vivo*, studies and through consecutive passages allow characterization of the tumor even after patient mortality. Although there are limitations, particularly related to the host environment, PDX is probably the closest currently available model to the human disease. Several studies in bladder (Pan et al., 2015), colorectal cancer, and lymphoma (Song et al., 2016) have shown the similarities between primary tumors and PDX, with a particular emphasis on genomic alterations. Importantly, a study on PDAC and hepatocellular carcinoma PDX suggested that the main differences in gene expression between primary tumors and xenografts are due to the difficulty of profiling the murine stroma using microarrays (Martinez-Garcia et al., 2014), as they measure human gene expression. With the advent of sequencing-based transcriptomic profiling, PDX offers an ideal setting to distinguish and study the interactions between the tumor and stromal cells. Indeed, sequencing profiles of a mix of human grafted cancerous and infiltrating mouse stromal cells can be analyzed separately *in silico* by unambiguously assigning each sequence to the human or mouse genome (Bradford et al., 2013). However, although PDX models are increasingly used in preclinical studies, they are insufficiently characterized, as few studies have addressed the question of their relevance as a model of the diversity of human disease (Witkiewicz et al., 2016). Finally, we expect that the integrated analysis of PDX multiomics profiles will reveal therapeutic targets for this disease.

RESULTS

PDX Establishment and Validation of the Model

Following suspicion of PDAC, the endoscopic ultrasound-guided fine-needle aspirates of non-resectable tumors or surgical samples of resectable tumors were used to generate subcutaneous xenografts in immunocompromised mice. Histological comparison of resected primary tumors with their correspondent PDX demonstrated extensive similarities (Figure S1A). Early passage of 29 patient-derived xenografts (30 xenograft samples in all) were used to generate genomic, epigenomic, and transcriptomic profiles (Figure 1A). In order to accurately analyze bulk xenograft samples, we developed a methodology that we termed SMAP (simultaneous mapping for patient-derived xenograft), which uses both the human and mouse genomes to distinguish reads from the tumor and stromal compartment, respectively (see Supplemental Information). The separation of species-specific RNA reads resulted in two transcriptomic profiles for each sample: one tumor profile based on human RNA sequences from the grafted tumor cells and one stromal profile from the mouse RNA sequences.

To validate PDX as a model of the primary tumor, the transcriptomes were compared to the virtually microdissected expression signatures that were recently proposed as associated with the tumor or stromal cells of primary human PDAC (Moffitt et al., 2015). The immune signature and the two stromal signatures (normal and activated) were predominantly expressed by the murine stromal cells, while the two cancer signatures (basal-like and classical) were expressed by the human tumor cells (Figures 1B and S1B). This clear distinction of the grafted human tumor cells and the recruited murine stromal cells provides the means to identify potential tumor-stroma interactions from the analysis of a bulk xenograft sample. The combined analysis of both murine and human transcriptomes highlighted several well-described tumor-stroma interactions, such as the activation of MET and insulin growth factor (IGF)1R in tumor cells by the stromal-expressed HGF and IGF, respectively (Figures 1C and S1C; Table S1). Interestingly, 9 out of 17 stromal genes shown in Figure 1C are part of the activated stromal signature previously defined in human primary tumors (Moffitt et al., 2015). Overall, these results illustrate the relevance of the PDX model, in particular, in the establishment of a dialog between the grafted cells and their host microenvironment.

Mirrored Tumor-Stroma Classification

In order to uncover the tumor diversity of PDAC using PDX, unsupervised analyses were carried out independently on each of the tumor-specific genome-wide molecular profiles: protein coding mRNA, long non-coding RNA, microRNA, and non-island and island CpG methylation. The resulting classifications consistently characterized two subtypes defined by the nearly identical sets of samples (Figures 2A and S2A–S2F; Table S2). This marked convergence was summarized in a consensus multiomics classification composed of two subtypes, basal (orange) and classical (blue), as well as two samples with discrepancies between their single-omics classification that will be referred to as outliers (gray) (Figure 2A). Although non-island methylation was consistent with the other single-omics, the island

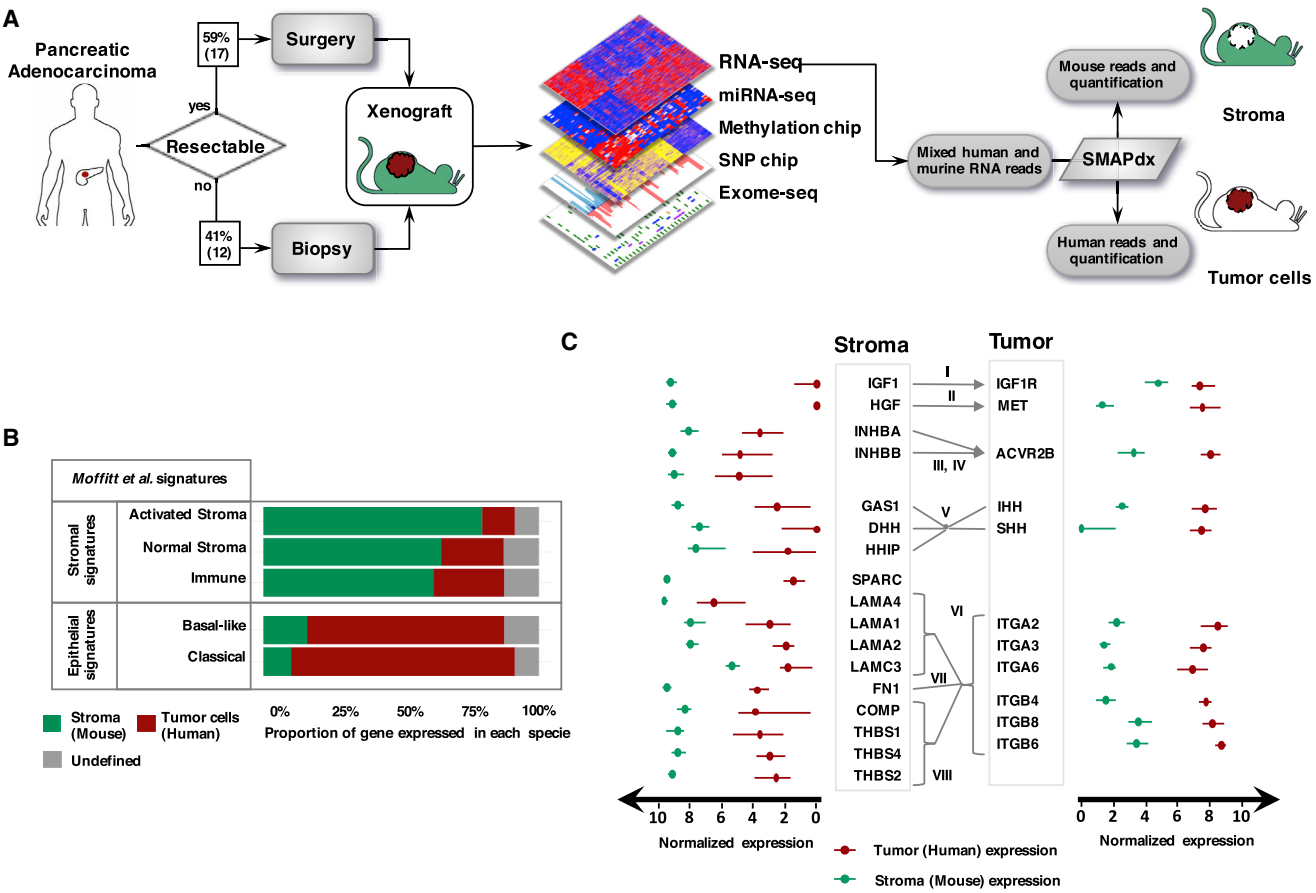

Figure 1. Patient-Derived Pancreatic Adenocarcinoma Xenograft Generation and Characterization

(A) Experimental design for systematic PDX generation followed by molecular tumor and stromal cell characterization. Numbers of biopsy and surgical samples are indicated.

(B) Expression of human primary PDAC stromal and tumor signatures in the mouse stroma or human tumor cells. Lateral stacked bars correspond to the number of genes in each signature that is specifically expressed in PDX by mouse cells (green), human cells (red), or neither (gray).

(C) Tumor (red) and stromal (green) expression of genes in pathways known to be involved in tumor/stroma cross-talk. Values shown are median expressions, and error bars indicate first and third quartiles. References: I (Bergmann et al., 1995), II (Qian et al., 2003), III (Lonardo et al., 2011), IV (Ohnishi et al., 2003), V (Tian et al., 2009), VI (Whatcott et al., 2013), VII (Topalovski and Brekken, 2016), and VIII (Farrow et al., 2009).

methylation classification revealed a subgroup of CIMP (CpG island methylator phenotype) tumors within the classical subtype (Figure 2B). Virtually, no genes were found to be significantly differentially expressed in association to the CIMP in this cohort (Figures S2G–S2I; Table S2). Moreover, the genes that were associated with the CIMP hypermethylated CpG were more often found to be underexpressed in all classical samples (64 of the 184 hypermethylated genes found significantly underexpressed in classical samples as compared to basal samples) than specifically underexpressed in CIMP samples (neither of the 2 genes were found to be underexpressed in CIMP samples). These results suggest that the CIMP is only one of the mechanism-silencing genes in classical samples, while the others are yet to be discovered.

Global genomic properties such as chromosomal instability index (CIN) or mutation rate showed no specific association with the classification (Figure 2B). Unsurprisingly, genomic alterations that are commonly found in PDAC (*KRAS* mutations, *SMAD4* losses, *CDKN2A* inactivation, *myc* amplification, etc.), were also widespread in PDX (Figure S2J). However, none of these alterations and none of any of the genomic alteration events, including potential gene fusions (Table S2), identified in this work were associated with the basal or classical subtype. As previously observed (Bailey et al., 2016), *TP53* showed a slightly higher mutation rate in the basal subtype, although with virtually no discriminative power. Besides the absence of subtype-specific single alterations, the unsupervised classification of copy number aberrations also showed no association (Figure S2K). This lack of genetic support for the two PDAC subtypes has been suggested in a larger series of patients using whole-genome sequencing (Bailey et al., 2016). However, the remarkable parallel between the transcriptome and methylome suggests that the main phenotypes in PDAC are epigenetically rather than genetically established.

Clinical and histopathological characterizations revealed that patients of the basal subtype were more often non-resectable,

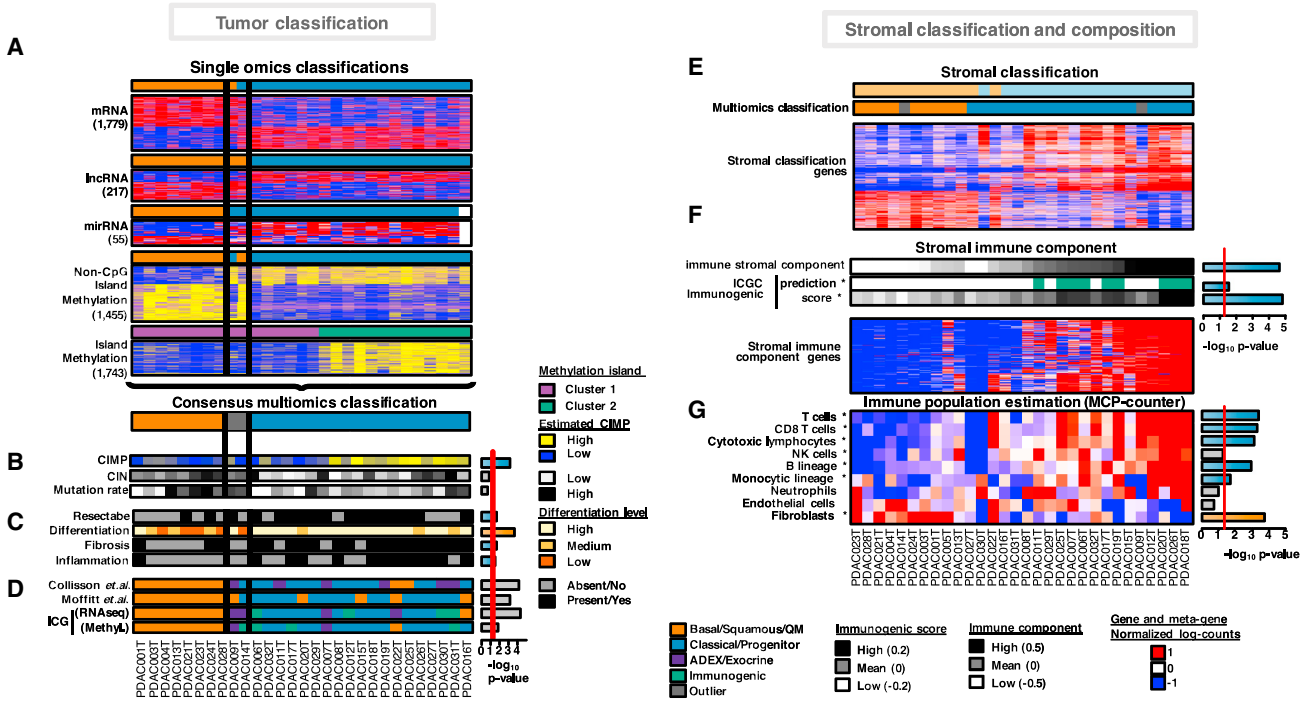

Figure 2. Tumor and Stroma Classifications

(A) Single-omics classifications and associated differential feature heatmaps used to define a consensus multiomics classification. Numbers in parentheses correspond to the number of differential features.

(B) Global epigenetic and genetic characteristics estimated from genome-wide assays. CIN, chromosomal instability index; CIMP, CpG island methylator phenotype.

(C) Clinical and histopathological characteristics.

(D) Primary human PDAC classification systems applied to the PDX tumor cell transcriptomes or methylation data (Methyl.). Lateral bars correspond to $-\log_{10}$ p value of Fisher's exact test of the association with the consensus multiomics classification (excluding outliers). Bars are colored when associated to a specific subtype (orange for basal; blue for classical) and significant ($p \leq 0.05$, indicated by red line).

(E) Consensus clustering applied to the stromal gene expression, generated from mouse RNA-seq reads. Heatmap represents expression values of all differentially expressed stromal genes between the two stromal subtypes.

(F) Immune stromal component sample projection and its contributing genes associated to the ICGC immunogenic subtype (prediction and score) applied to the stromal transcriptomes.

(G) Estimated level of infiltration of seven immune and two other stromal populations as computed by MCPcounter. Lateral bars correspond to $-\log_{10}$ p value of the association with the consensus multiomics classification (excluding outliers; Fisher's exact test or ANOVA). Bars are colored when associated to a specific subtype (orange for basal; blue for classical) and significant ($p \leq 0.05$). *$p \leq 0.05$, significant association with the stromal immune component (Pearson's correlation or ANOVA). All classifications and components analysis shown are based on unsupervised analysis of the associated datasets. Heatmaps show expression/methylation values of the genes/CpG most associated with the unsupervised classification or component. All heatmaps are shown with the same samples in the same order.

had a marginally lower median survival, and presented a less differentiated tumor (Figures 2C and S2L), altogether indicating a more aggressive phenotype. Conversely, classical tumors were more frequently resectable, presented a higher level of differentiation, and were often associated with fibrosis and inflammation. In order to compare these PDX-based subtypes with currently available human PDAC classifications, methylome and gene expression classifiers were constructed from three different public datasets (Collisson et al., 2011), (Moffitt et al., 2015), ICGC methylation (Nones et al., 2014) and RNA sequencing (RNA-seq) (Bailey et al., 2016). All published PDAC classification systems were in agreement with the proposed multiomics classification, thereby illustrating the reliability of PDX to model PDAC diversity (Figures 2D and S3A–S3D). Altogether, our analysis on cancer cells using either PDX or human PDAC classifications reveals the presence of two clinically relevant types of PDAC.

Unsupervised analysis of the stromal transcriptomes reconstructed from the murine RNA sequences also revealed two types of stroma with a strong agreement with tumor subtypes (Figure 2E). In order to evaluate this remarkable echo in the diversity of the tumor cells and of their stroma, the tumor and stroma PDAC PDX subtypes were predicted in four public datasets of human primary PDAC. To do so, we derived a tumor and a stromal gene signature predictive of PDAC subtypes based on tumor and stromal expression, respectively. A minor overlap was found between the genes of these signatures, a majority of which encoded cell communication proteins or extra-cellular components (e.g., semaphorins, cytokines; Table S2). The stromal and tumor subtype prediction made by these gene

signatures significantly matched in all four primary human tumor datasets, which confirms the mirrored tumor-stromal classification observed in xenografts (Figure S3E).

Interestingly, two recent studies on bulk primary human pancreatic tumors proposed a classification that was suggested to be linked to the stromal composition. The first, by Moffitt et al., described an activated stroma that was linked to a poor outcome (Moffitt et al., 2015) and recently associated with the basal subtype (Bailey et al., 2016). The second was the immunogenic group, which was suggested to be driven by a strong infiltration of immune cells. In order to further characterize the stroma of PDX, a blind source separation algorithm, independent component analysis, was used to extract two components from the stromal transcriptomes (Table S2). The first component was weakly associated with the basal subtype and mostly composed of genes that define the proposed activated stroma of primary PDAC (Moffitt et al., 2015) (Figure S3F). The genes contributing to this component observed in the stroma of xenograft suggest a gradient in stromal activation. Similar to observations in primary human PDAC, the xenografts with a strong activation of their stroma have a marginal tendency to be associated with patients with lower survival (Figure S3G). The second component was strongly associated with the classical subtype as well as with the immunogenic class predictor applied to the stroma (Figure 2F). The immune aspect of this component was supported by its correlation with the infiltration of several populations of immune cells estimated using MCPcounter (Becht et al., 2016) (Figure 2G). Remarkably, these results show that, although the mouse hosts are immunodeprived, PDX tumor models are able to reproduce an immune-related phenotype observed in human primary tumors.

Basal Subtype Characterization

The precise sequence-based dissociation of tumor and stroma transcriptomic profiles offers the possibility to rigorously analyze the carcinogenic processes of tumor cells in a subtype-specific approach (Table S3). The basal subtype showed significant deregulations in oncogenic-related pathways and, in particular, a strong overexpression of cell-cycle genes (Figure 3A). The upregulation of the glycolysis in basal tumor cells is in line with a recent description of a group of glycolytic PDAC cell lines associated with a characteristic mesenchymal phenotype (Daemen et al., 2015). Several pathways were also associated with a differential methylated pattern as well as miRNA-based deregulations. This supports the hypothesis that PDAC diversity and the specificities in carcinogenic development of each subtype are epigenetically rather than genetically driven.

In addition to the description of basal tumor cell pathways, the differential analysis of basal stromal pathways was also carried out. The genes involved in focal adhesion and axon guidance pathways, which imply complex interactions with the surrounding tissues, were overexpressed by the tumor and stromal compartments. Along with the enrichment of basal PDX in fibroblasts (Figure 2G), this result suggests a basal-specific communication between tumor cells and adjacent fibroblasts, which is in agreement with recent observations in PDAC of the role of cancer-associated fibroblasts in axon guidance signaling (Secq et al., 2015). In order to validate the transcriptional activation of these pathways in human primary PDAC, an identical pathway analysis was performed on three independent datasets (Figure 3A). The results consistently showed that human basal PDAC activated all of the pathways highlighted in basal PDX. Moreover, the comparison between basal cancer and normal pancreatic transcriptomes showed that these pathway upregulations were cancer specific. Figure 3B schematically illustrates the means by which transcriptional and epigenetic alterations stimulate the highly deregulated WNT pathway. Wnt signaling is potentially activated by tumor cells in an autocrine manner through the upregulation of several WNT ligands, as well as in a paracrine manner by the stromal upregulation of distinct WNT ligands. Finally, the analysis of the methylation patterns suggests a sustained activation of the entire pathway as shown by aberrant methylation of effectors at nearly every step of the signaling cascade as well as of inhibitors of the pathway (Figure S4A).

Classical Subtype Characterization

The analysis of transcriptionally upregulated genes in classical PDX revealed the activation of many pathways (Figure 4A). The upregulation of all of the highlighted pathways was verified in an equivalent differential analysis on human primary PDAC. Importantly, several of these were also found to be active in normal pancreatic samples, suggesting an aberrant differentiated phenotype. Interestingly, a majority of classical-specific pathways relate to either pancreatic digestive function (fat and protein digestion, pancreatic and bile secretion), metabolite transport (fat and protein absorption, small molecule transport), or metabolic pathways (glucose, fructose, mannose, arginine, proline, linoleic, and arachidonic acid metabolism). These results suggest that Classical tumor cells acquire cellular functions usually imputed to other gastrointestinal tissues (*e.g.* enterocytes), in addition to retaining some level of pancreatic digestive function. This is in line with the previous description of the Classical subtype as Progenitor, although we speculate it may acquire some characteristics of a more general gastrointestinal progenitor. Unlike the previously proposed exocrine-like or ADEX PDAC subtypes, we observe here that the Classical subtype maintains a lower level of a more general digestive activity, including product breakdown and uptake that could be used to fuel high metabolic needs. Altogether, we describe the Classical subtype as closer to normal pancreatic tissue than the Basal subtype yet, we do not identify any acinar-like or any differentiated pancreatic subtypes which would only harbor functions and markers of the exocrine or endocrine pancreas.

In order to further characterize the molecular phenotypes of these PDXs, extensive metabolomics profiles, including lipidomics, were generated. Differential analysis of metabolite quantifications supported this hypothesis by demonstrating a general increase in REDOX-related metabolites (Figure S4B; Table S4), previously associated with well-differentiated PDAC cell lines (Daemen et al., 2015). The potential digestive activity was particularly demonstrated by the decline in triacylglicerols associated with an increased lipase expression and an increased level of fatty acids (Figure 4B). In addition, classical tumors also displayed an increase in several glycerophospholipids

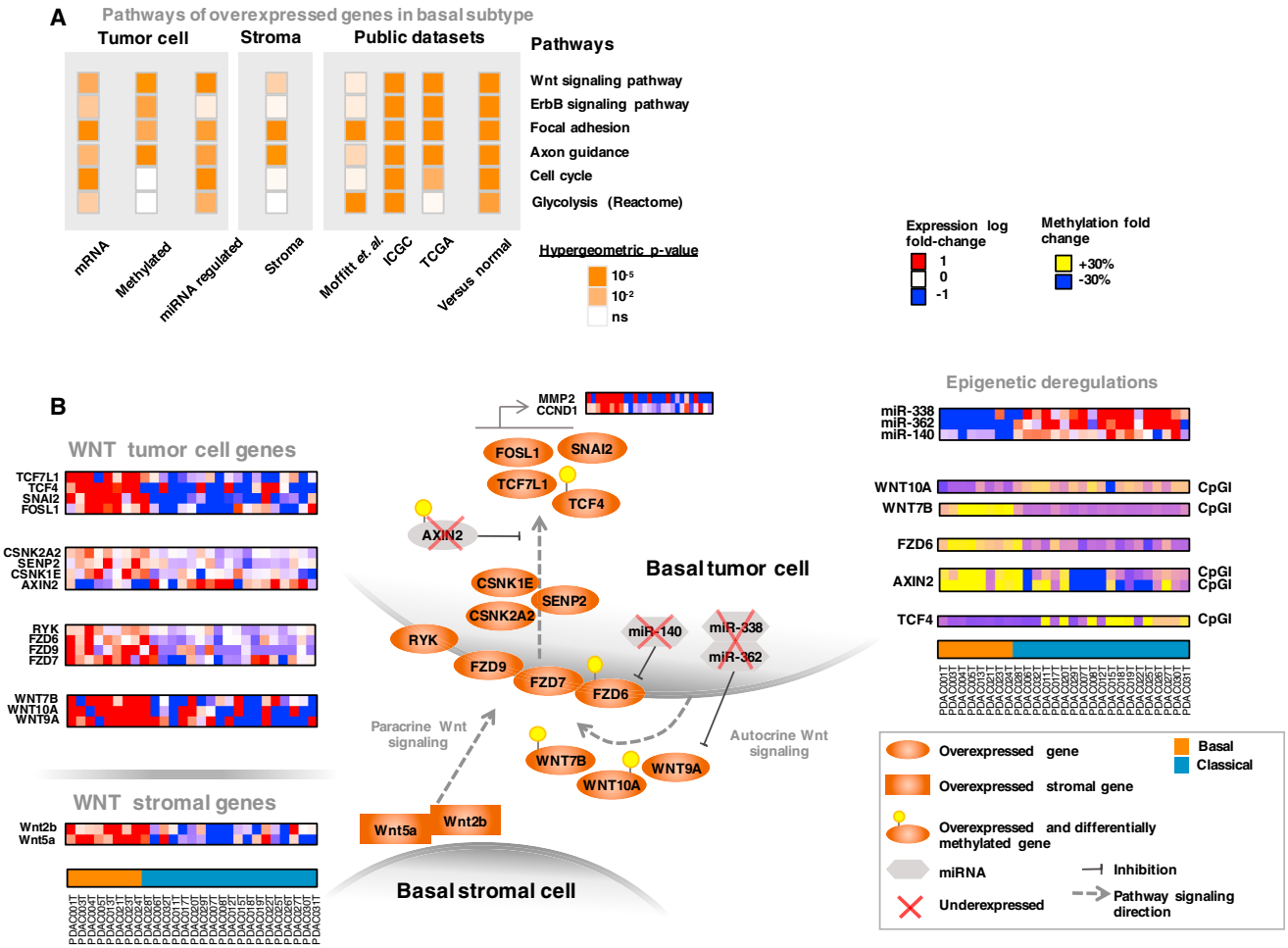

Figure 3. Basal Epigenetically Deregulated Pathways

(A) Basal pathway enrichment of: overexpressed genes (mRNA), overexpressed and differentially methylated genes (Methylated), overexpressed genes that are targets of underexpressed microRNA (miRNA regulated), genes overexpressed in the stroma of basal tumors (Stroma), overexpressed genes in the basal tumors of the Moffitt et al. (2015) dataset (Moffitt et al.), the ICGC dataset (ICGC), and the TCGA dataset (TCGA), and genes overexpressed in basal tumors compared to normal pancreatic samples (Versus normal). Pathway definition originates from the Kyoto Encyclopedia of Genes and Genomes (KEGG) database unless specified otherwise.

(B) Schematic illustration of the tumor and stromal deregulation of the WNT signaling pathway. Ellipses represent genes and hexagons miRNA found to be overexpressed (orange) or underexpressed (gray and crossed) in basal PDX tumors. Yellow circles indicate methylation-associated deregulation of expression. Rectangles represent genes overexpressed in basal PDX stroma. Blue-red heatmaps represent expression values of genes and miRNA. Blue-yellow heatmaps represent methylations values of CpG associated with genes. The CpGI annotation indicates that represented CpG methylation level originates from a CpG island. All heatmaps are shown with the same samples in the same order.

(Figure S4C), altogether indicating a broad deregulation of the lipid metabolism, as suggested in a previous metabolomics study on PDAC cell lines (Daemen et al., 2015).

Figure 5 shows a partial view of the range of small molecule transporters overexpressed in classical samples, which include the upregulation of the glucose (*SLC2A2*) and glutamine (*SLC1A1*) transporters, which are strongly hypomethylated in classical samples (Figure S4D). Glutamine is a necessary nitrogen donor for the initial steps of nucleotide biosynthesis. Interestingly, the upregulation and epigenetic deregulation of the glutamine transporter in classical tumors is associated to a strong increase in two nucleotides, inosine monophosphate (IMP) and uridine monophosphate (UMP) (Figure S4E). Cholesterol transporters were also significantly upregulated; in particular, the overexpression of the intestinal cholesterol uptake regulator *NPC1L1* was associated to extensive hypomethylation (Figure 5). Aberrant cholesterol uptake has been recently implicated in the proliferation and survival of pancreatic cancer cells (Guillaumond et al., 2015). Metabolomics profiling revealed a significantly higher level of cholesteryl ester in classical PDX (Figure 5), supporting an increased absorption activity. Moreover, the analysis of the stroma of classical tumors highlighted the upregulation of genes involved in lipid metabolism and cholesterol synthesis, as well as the master regulators of lipid

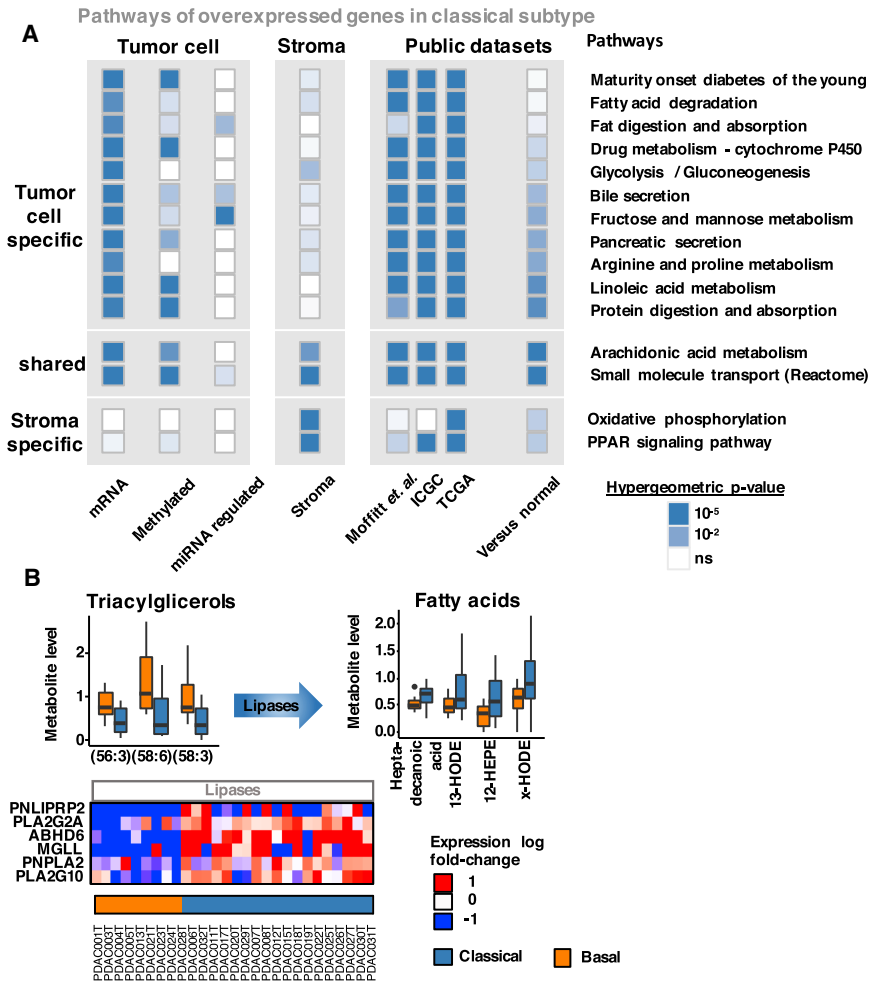

Figure 4. Classical Signaling and Metabolic Pathways

(A) Classical pathway enrichment of: overexpressed genes (mRNA), overexpressed and differentially methylated genes (Methylated) overexpressed genes that are targets of underexpressed microRNA (miRNA regulated), genes overexpressed in the stroma of classical tumors (Stroma), overexpressed genes in the classical tumors of the Moffitt et al. (2015) dataset (Moffitt et al.), the ICGC dataset (ICGC) and the TCGA dataset (TCGA), and genes overexpressed in Classical tumors compared to normal pancreatic samples (versus normal). Pathways are ordered by their tumor specificity compared to normal pancreatic samples and to the stroma. Pathway definition originates from the KEGG database, unless specified otherwise.

(B) Pancreatic lipase activity. Boxplots show the levels of the putative metabolic substrates (triacylglicerols, left) and products (fatty acids, right) of lipases in basal and classical samples. Expression of lipases is represented as a heatmap.

and cholesterol homeostasis, namely, *PPARG* and *NR1H3* (LXRα). Altogether, these results suggest an active cross-talk involving the stromal synthesis of cholesterol associated with aberrant nutrient uptake by classical tumor cells.

In order to validate the predicted compartment-specific expression of genes of interest, immunohistochemical staining was performed. As a control, *MUC17*, which was expressed by classical tumor cells displayed no protein expression in basal tumors, as expected (Figures S5A and S5B). Immunohistochemical staining of PPARG and its target FABP5 confirmed transcriptomic data by validating their expression in classical stromal cells (Figures S5C and S5D).

Evidence of Potential Therapeutic Targets

Despite the absence of any specific druggable genetic alterations, the integrative multiomics analysis uncovered epigenetically deregulated pathways in PDAC subtypes with high potential druggability (e.g., WNT, *EGFR*, *PPARG*, small molecule transporters). In particular, our integrated analysis examined the stroma as well as the epigenetic deregulation of cholesterol metabolism and uptake. Moreover, cholesterol metabolism was recently associated with pancreatic cancer in cellular and epidemiological studies (Chen et al., 2015; Guillaumond et al., 2015). As a proof of concept for defining therapeutic targets from the integrated multiomics analysis of PDX, we selected the highly epigenetically deregulated *NPC1L1*, for which an efficient inhibitor is clinically available: Ezetimibe. DNA demethylation using 5-Aza-2′-deoxycytidine confirmed the epigenetic regulation of *NPC1L1* (Figure S6A). Immunohistochemical staining confirmed the protein expression of *NPC1L1* and its correlation with mRNA levels, overall showing higher levels in classical tumors (Figures 6A and S6B).

Sensitivity analysis of Ezetimibe on the survival of 4 basal and 3 classical PDX-derived cell cultures expressing different levels of *NPC1L1* revealed that all PDAC cells are sensitive to the inhibitor, while the treatment had little to no effect on fibroblasts (Figures 6B and S6C). However, as Ezetimibe functions as a competitor of cholesterol, cells expressing lower levels of *NPC1L1* (i.e., Basal) were highly sensitive, while cells with high levels of *NPC1L1* (i.e., Classical) required greater inhibitor quantities (Figure 6C). This result suggests that *NPC1L1* and, by extension, the cholesterol metabolism have a major role in both Basal and Classical PDAC. In addition, the combination of gemcitabine with Ezetimibe did not affect the cytotoxic effect of gemcitabine in PDAC cells (Figure S6D).

In order to study the specificity of *NPC1L1* inhibition on PDAC survival, targeted small interfering RNA (siRNA) knockdown was performed. This genetic approach revealed a dramatic effect on the survival of the siRNA-transfected cells validating the role of *NPC1L1* as an original therapeutic target (Figure 6D). The knockdown of *NPC1L1* made cells resistant to high levels of Ezetimibe, providing evidence for the specificity of the

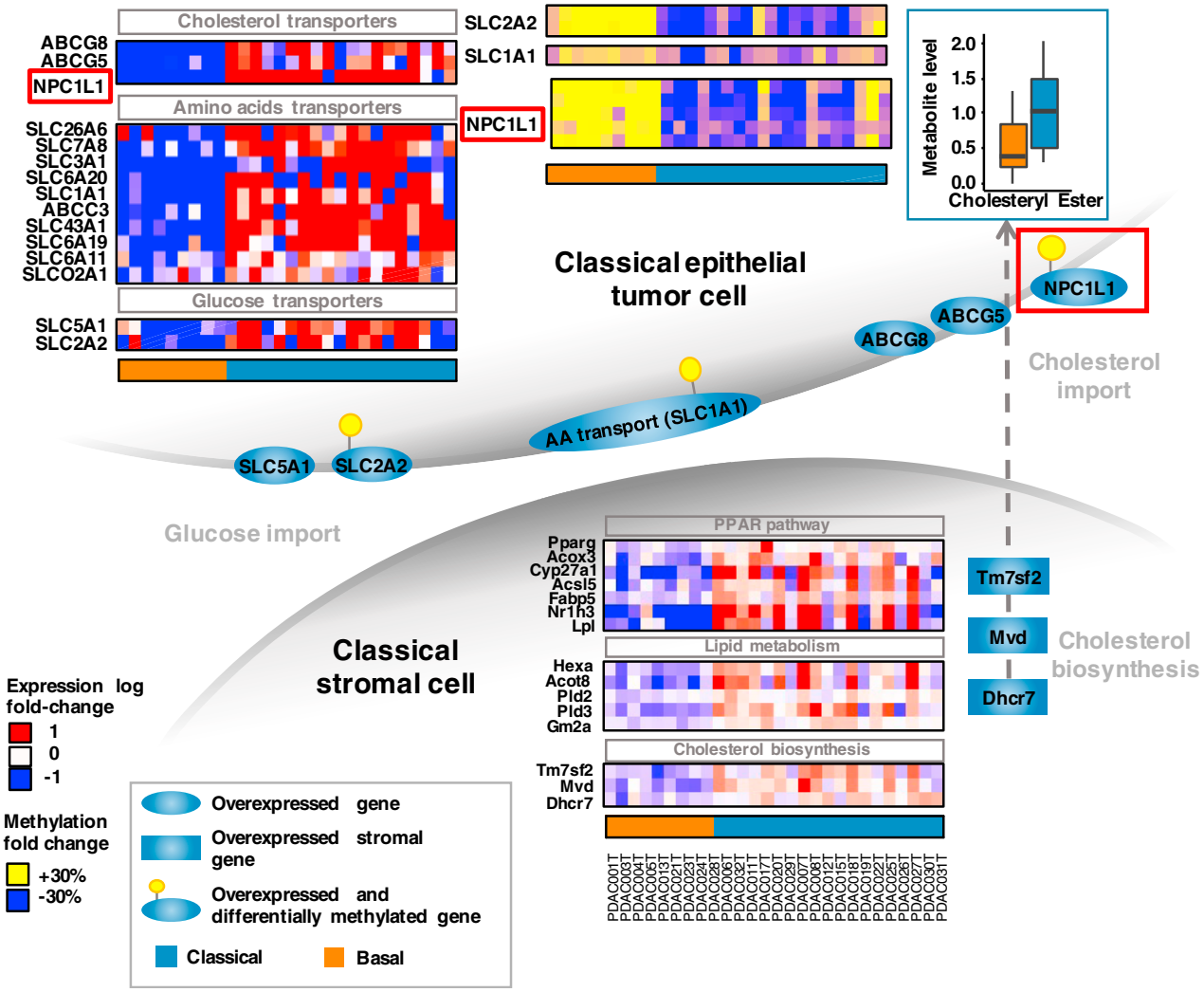

Figure 5. Classical Deregulated Tumor-Stroma Signaling Cross-Talk

Schematic illustration of the overexpressed transporters and stromal pathways in classical tumors. Ellipses represent genes overexpressed (blue) in classical PDX tumors. Yellow circles indicate methylation-associated deregulation of expression. Rectangles represent genes overexpressed in classical PDX stroma. Boxplots show the levels of cholesteryl ester in basal and classical samples. Blue-red heatmaps represent expression values of genes and miRNA. Blue-yellow heatmaps represent methylations values of CpG associated with genes. Arrows indicate the hypothetical flow of cholesterol. All heatmaps are shown with the same samples in the same order.

treatment (Figures S6E and S6F). We then derived spheroids and organoids from PDX and treated these structures with Ezetimibe for 3 and 4 days, respectively, as shown in Figures 6E and 6G. Ezetimibe treatment resulted in a significant effect on their growth, as measured by cell viability (Figures 6F and 6I) and volume change (Figure 6H). Finally, we performed a preclinical analysis by treating two PDXs with Ezetimibe (5 mg/day) in 200 μL corn oil by a daily intraperitoneal (i.p.) injection to confirm the *in vitro* results. As shown in Figure 6J, PDAC019T (classical) and PDAC003T (basal) samples efficiently responded to the treatment by reducing their growth. Based on these *in vitro* and *in vivo* results, we conclude that *NPC1L1* is a highly effective therapeutic target for treating PDAC using Ezetimibe.

DISCUSSION

We report in this work the use of PDXs to profile both resectable as well as non-resectable PDAC. We found that PDXs obtained by biopsied PDAC are frequently associated with a more aggressive phenotype, suggesting that studies profiling PDAC still present a bias. Moreover, one advantage of a xenograft is to combine transformed tumor and stromal cells from distinct species, resulting in the ability to investigate cancer and stromal molecular profiles independently. Analysis of tumor-cell-specific molecular profiles allowed the examination of epigenetic and transcriptomic profiles, separately from non-neoplastic signals. Conversely, the absence of relationship between the consensus multiomics classification and

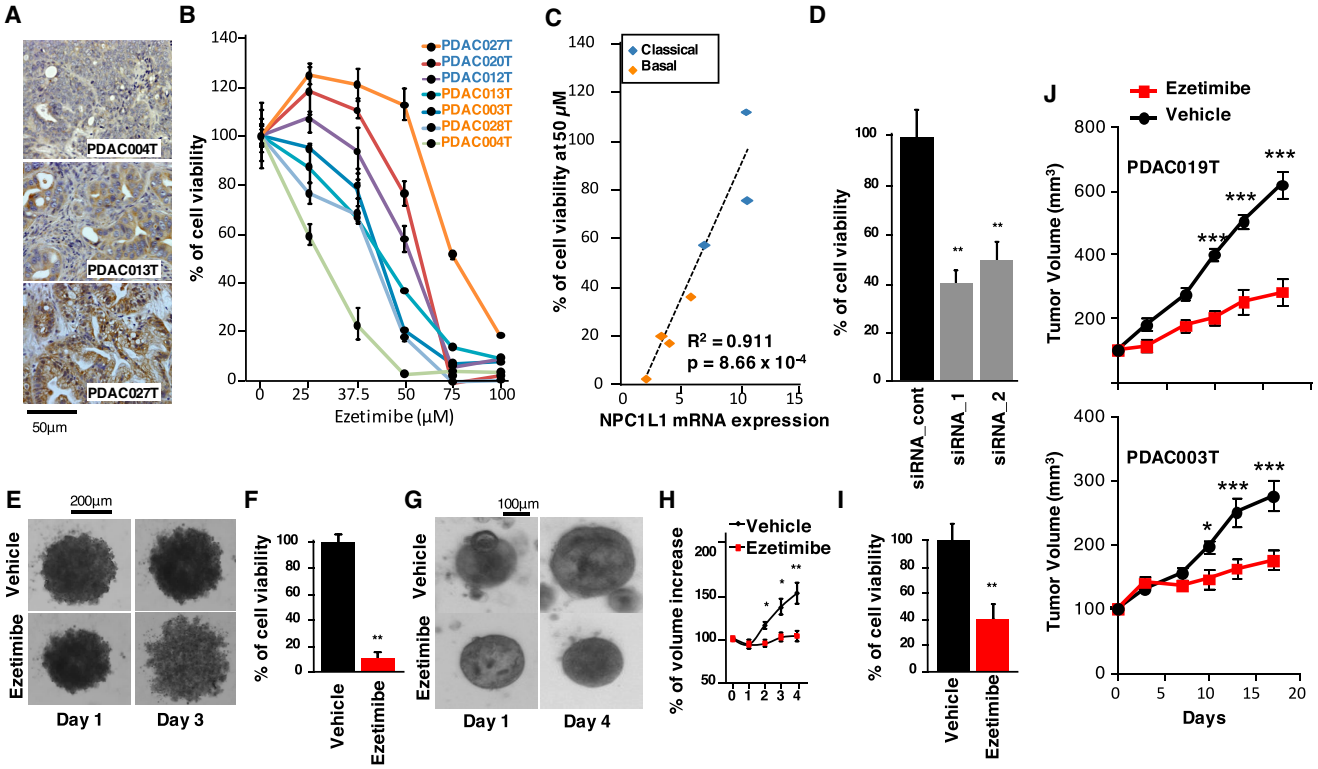

Figure 6. *NPC1L1* Is a Therapeutic Target for Treating PDAC

(A) Immunohistochemical staining of NPCL1L.

(B) Ezetimibe sensitivity of 7 PDX-derived cell lines. Dose-response curves after 72 hr of Ezetimibe treatment. The level of cell viability is represented as a percentage to the vehicle-treated control. Error bars represent SEM; n = 6.

(C) Correlation between survival percentage of Ezetimibe at 50 µM and *NPC1L1* mRNA expression for the 8 PDXs with Spearman correlation.

(D) Effect of knockdown *NPC1L1* with siRNA. si_RNA_1 and siRNA_2 directed against *NPC1L1* were transfected into PDAC012T, and survival was measured 72 hr later. Data are expressed as a percentage of siRNA_control (cont)-transfected cells.

(E and F) Effect of Ezetimibe on spheroid growth is indicated.

(E) Representative picture of the PDAC012T-derived spheroids treated with Ezetimibe (50 µM) or vehicle after 3 days.

(F) Cell viability of spheroids was measured by CellTiter Glo and expressed as percentage of the vehicle-treated spheroids. **$p < 0.01$.

(G–I) Effect of Ezetimibe on organoid growth is indicated.

(G) Representative picture of the PDAC012T-derived organoids treated with Ezetimibe (50 µM) or vehicle after 4 days.

(H) Calculated volume of organoids treated with Ezetimibe. *$p < 0.05$; **$p < 0.01$.

(I) Cell viability of organoids was measured by CellTiter Glo and expressed as percentage of the vehicle-treated organoids.

(J) Two PDXs were treated with 5 mg/day of Ezetimibe or with vehicle for 17 days by i.p. injections (n = 3 per group). *$p < 0.05$; ***$p < 0.001$, in two-way ANOVA with Bonferroni post-test (mean ± SEM).

genomic alterations, which was previously proposed, is unambiguously confirmed in this work. This is a crucial confirmation, since it supports the idea of an epigenetic identity for PDAC subtypes. The most likely explanation for this observation is that genetic mutations, amplifications, and deletions are involved in the transformation process of PDAC, whereas the clinical outcome, response to treatments, and the phenotype of the tumors are controlled at the epigenetic level. This observation is of obvious clinical relevance, since emerging epigenetic drugs can be used to target these tumor characteristics and, therefore, opens a promising avenue in the treatment of PDAC patients. While preliminary genomic analysis suggested that genetic alteration could define therapeutic options (Witkiewicz et al., 2015), more recent studies found no associations between any genetic alterations and therapeutic responses on a large number of drugs (Knudsen et al., 2017; Witkiewicz et al., 2016).

Based on the analysis of PDX, we identified two major subtypes with extensive similarities to the basal and classical human PDAC subtypes. The specific analysis of the tumor cell profiles underlined the homogeneity of basal samples while highlighting the diversity of the classical subtype. For instance, while CIMP PDACs have been described (Ueki et al., 2000), we found that this phenotype corresponds to a subdivision of classical PDAC exclusively. Overall, the two molecular subtypes describe two distinct PDAC development patterns: a dedifferentiated basal subtype, highly glycolytic and with features associated with epithelial-mesenchymal transition, and a subtype with more general digestive differentiation features reminiscent of an aberrant gastro-intestinal progenitor. In addition to having distinct and

specific signaling exchanges with their stroma, a broad homogeneity among all samples can be observed in some major tumor-stroma pathways (e.g., HGF, IGF, and Hedgehog). Despite the PDX being hosted in immunodeprived mice, we found a subgroup of samples in the classical PDX group with extensive immune infiltration that strongly correlated with the immunogenic subtype described in primary PDAC (Bailey et al., 2016). Our observations indicate that this subgroup is broadly driven by its stromal content and is, in fact, a "classical inflammatory infiltrated" subtype instead of a specific subtype by itself. Although these models are not suitable to study immune therapy, these results show the extent to which xenografts can reproduce primary PDAC phenotypes, including interaction with the immune microenvironment. Importantly, athymic NMRI nude mice (*Foxn1nu*) lack conventional T cell development, but this does not preclude extrathymic maturation such as intestinal T cell differentiation, which likely explains the extensive infiltration of the immunogenic-like PDX. Although nude mice lack thymus-dependent lymphocytes, other immune cell populations such as macrophages, natural killers and B cells are present and functional. Given the potential of PDX to reproduce an immunogenic PDAC subtype in a model with an only partial immune landscape, new developments in animal models, in particular humanized mice, can be expected to greatly improve the present model and potentially be used to investigate immune therapies.

In addition to greatly improving the multiomics description of tumor-specific altered pathways, the precise distinction of tumor and stromal cells in the same samples enabled analysis of cross-talk at the genome-wide level. The simple description of the most expressed genes in each compartment highlighted known molecular dialogs between tumor cells and their stroma. The role of PDAC stroma on tumor survival and growth is not settled. It was previously suggested that the stroma plays a major role in the resistance to the PDAC treatments, because it acts as a mechanical barrier impeding the access of the drugs and also inhibits the formation of vessels. Therefore, it seemed important to combine agents against cancer cells with compounds targeting the stroma to improve efficiency. Accordingly, recent results encourage going forward in this way. In fact, initial testing of the Hedgehog signaling pathway inhibitor IPI-926 demonstrated a promising transient effect on the tumor microenvironment, leading to improved drug delivery and an association with improved survival in mice treated with both IPI-926 and gemcitabine (Olive et al., 2009). Mouse models of PDAC deficient in Sonic Hedgehog (Rhim et al., 2014) demonstrated that Hedgehog inhibition leads to an absence of tumor stroma and an abundance of intratumoral blood vessels yet increases tumor aggressiveness and metastasis. Another potential stroma-targeting therapy relates to glycosaminoglycan hyaluronan, which is overrepresented in PDAC stroma and which can be degraded by hyaluronidase. Notably, treatment with PEGPH20, a PEGylated human recombinant hyaluronidase, induces a rapid perfusion increase, leading to the inhibition of growth when combined with chemotherapy in mouse PDAC models (Walker et al., 2015). While the outcome of stroma-targeting therapies remains unknown, major signaling pathways driving PDAC have been shown to be stimulated by the non-transformed cells composing its microenvironment. Our work revealed the potential sustaining role of the stroma as subtype specific. Indeed, the analysis of the recruited stroma diversity revealed the unidentified subtype specificity of the stroma through the discovery of convergent tumor/stromal classifications, which was verified in four different datasets of primary tumors. This is, to some extent, dissimilar to the activated stroma previously described (Moffitt et al., 2015) as subtype independent. Overall, our results show that the stroma, originating from surrounding host cells, is closely associated with the phenotype of the tumor indicating that the composition and function of the tumor microenvironment may be trained by tumor cells.

A major advantage of the PDX model is that it is a perpetual source of living material conserving original biological characteristics. Indeed, each PDX can be molecularly analyzed and concomitantly used for testing biological hypotheses or putative therapeutic targets derived from these analyses. In this work, we describe several subtype-specific pathways, thereby highlighting potential targeted therapies. We used *NPC1L1*, a transporter of cholesterol, as a proof of concept of an original candidate to be targeted for treating PDAC. The function of this gene can be inhibited by a specific inhibitor, Ezetimibe, which has been routinely used for the treatment of hypercholesterolemia. While no studies describe the association of *NPC1L1* or its inhibitor with pancreatic cancer, statins (used for the treatment of hypercholesterolemia) were shown in epidemiological studies to reduce the risks of pancreatic cancer (Walker et al., 2015) and to improve survival (Huang et al., 2016; Wu et al., 2015). Preclinical tests demonstrated that using the specific inhibitor Ezetimibe or genetic knockdown approaches results in a dramatic effect on the survival capacity of PDAC cells and on the growth of spheroids and organoids *in vitro* and of PDX *in vivo*. Finally, we also demonstrated that Ezetimibe treatment does not affect the cytotoxicity of gemcitabine, suggesting that patients could be treated with an inhibitor of the *NPC1L1* transporter in combination with a conventional anticancer drug without influencing its effect. Altogether, our data demonstrate that *NPC1L1* is an interesting and promising therapeutic target.

In conclusion, the data presented in this work reveal that PDX is a suitable model for preclinical studies, representing the diversity of the primary cancers in which the stroma is reconstituted. Its multiomics analysis is a rich source of novel and reliable therapeutic targets for treating patients with PDAC.

EXPERIMENTAL PROCEDURES

PDXs

Three expert clinical centers collaborated on this project after receiving ethics review board approval. Patients were included in this project under the Paoli-Calmettes Institute clinical trial number 2011-A01439-32. Consent forms of informed patients were collected and registered in a central database. The tumor tissues used for xenograft generation were deemed excess to that required for the patient's diagnosis. PDAC tissue from surgical samples was fragmented, mixed with 100 μL Matrigel, and implanted with a trocar (10G; Innovative Research of America, Sarasota, FL) in the subcutaneous right upper flank of an anesthetized and disinfected male NMRI-nude mouse. Samples obtained from endoscopic ultrasound-guided fine needle aspiration (EUS-FNA) were mixed with 100 μL of Matrigel (BD Biosciences, Franklin Lakes, NJ) and injected in the upper right flank of a male nude mouse (Swiss Nude Mouse Crl:NU(Ico)-Foxn1nu; Charles River Laboratories, Wilmington, MA) for the first implantation. When xenografts reached 1 cm^3, these were removed

and passed to NMRI-nude mice in the same manner as surgical samples. In total, 30 xenografts from 29 different patients were generated, and early passages were used for large-scale molecular profiling.

Genome-wide Profiles and Data Availability

Genotype data from whole-exome sequencing have been deposited at the European Genome-phenome Archive (EGA; http://www.ebi.ac.uk/ega/), which is hosted by the EBI, under accession number EMBL-EBI: EGAS00001001928. Other datasets are available on ArrayExpress (http://www.ebi.ac.uk/arrayexpress): SNP data are available under accession number EMBL-EBI: E-MTAB-5006, Methylation data are available under accession number EMBL-EBI: E-MTAB-5008, miRNA sequencing data are available under accession number EMBL-EBI: E-MTAB-5018, and mRNA sequencing data are available under accession number EMBL-EBI: E-MTAB-5039. Sequencing datasets were processed using SMAP (see Supplemental Experimental Procedures) to separate mouse and human reads. In addition to raw data, all processed data produced by and used in this study are available through our institutional web portal (http://cit.ligue-cancer.net/pacaomicsdata-web-page), and simple gene-level queries for expression and methylation are available using a custom application (http://cit-apps.ligue-cancer.net/pdac.pacaomics).

Public Dataset Comparison

ICGC methylation chips, RNA-seq, and microarray gene expression datasets were downloaded from the ICGC data portal (dcc.icgc.org, release 20). TCGA data were downloaded through the Broad Institute TCGA Genome Data Analysis Center (GDAC) firehose tool (gdac.broadinstitute.org, 20160411 data snapshot). Other datasets were downloaded from the provided GEO entries GSE71729 (Barr et al., 2012, 2010; Moffitt et al., 2015) and GSE17891 (Collisson et al., 2011; Martínez-Arranz et al., 2015; Nones et al., 2014). All non-cancer samples were removed from each dataset. Expression datasets were then centered gene-wise. Centroid classifiers were built for each dataset defining a classification using a Pearson-based approach described in previous work (Bailey et al., 2016; Guinney et al., 2015; Marisa et al., 2013)

Primary Cell Cultures and Sensitivity

Primary cell cultures were obtained from PDX. Ezetimibe was obtained from Selleckchem (ref. S1655). Tissues were split into several small pieces and processed in a biosafety chamber. Five thousand cells per well were plated in 96-well plates in serum-free defined media (SFDM) medium. The RNA profile of each cell culture showed a contamination in murine cells of less than 3%. Twenty-four hours later, the media were supplemented with increasing concentrations of Ezetimibe and incubated for an additional 72-hr period. Cell viability was estimated with the PrestoBlue (Invitrogen, Grand Island, NY) reagent. Each experiment was done in triplicate and repeated at least three times. Six increasing concentrations of Ezetimibe were used ranging from 0 μM to 100 μM.

Spheroid Sensitivity to Ezetimibe

Fifteen thousand cells per well were seeded in 96-well round-bottom plates with medium containing 20% methylcellulose (Sigma-Aldrich, St. Louis, MO, USA). After 48-hr incubation, cells with spheroids of uniform size and shape were incubated with 50 μM Ezetimibe during 72 hr. Spheroid growth was monitored for 96 hr by taking microphotographs every day or assessed with the CellTiter-Glo 3D kit at the end of the treatment according to the manufacturer's instructions (Promega, Madison, WI). Values were normalized and expressed as the percentage of the control treatment (DMSO, 0.05%).

Pancreatic Organoid Generation and Treatment with Ezetimibe

Organoid suspensions obtained from fresh tissue samples were placed into a 12-well plate coated with 100 μL GFR Matrigel. Media were replaced every 2–3 days. Twenty-four hours after seeding, organoids were incubated with 100 μL pancreatic organoid feeding media (POFM) supplemented with 50 μM Ezetimibe or 100 μL POFM supplemented with vehicle (0.5% DMSO) into 96-well plates coated with 15 μL Matrigel GFR. Organoid growth was monitored for 96 hr by taking microphotographs every day or assessed with the CellTiter-Glo 3D kit at the end of the treatment. Values were normalized and expressed as the percentage of the control.

Treatment with Ezetimibe of PDX *In Vivo*

We transplanted two PDX samples (PDAC019T and PDAC003T) subcutaneously into 6-week-old male Swiss nude mice (Crl: Nu(lco)-Foxn1nu; Charles River Laboratories, Wilmington, MA). Each PDX sample was inoculated into six nude NMRI mice that were randomized for treatment (n = 3) and vehicle (n = 3). When the PDX reached 100 mm^3, we started the treatment with Ezetimibe or vehicle and followed their growth for 17 days. Ezetimibe was prepared as a solution of 250 mg/mL in ethanol and then resuspended in corn oil at 25 mg/mL, and 200 μL was administered in i.p. injections every day. Tumor size was measured with a Vernier caliper twice weekly, and the tumor volume was calculated with the equation $v = (length/width^2)/2$.

DATA AND SOFTWARE AVAILABILITY

The accession number for exome sequencing reported in this paper is EMBL-EBI: EGAS00001001928. The accession number for SNP arrays reported in this paper is EMBL-EBI: E-MTAB-5006. The accession number for the ethylation array reported in this paper is EMBL-EBI: E-MTAB-5008. The accession numbers for miRNA-seq and RNA-seq reported in this paper are EMBL-EBI: E-MTAB-5018 and E-MTAB-5039, respectively.

SUPPLEMENTAL INFORMATION

Supplemental Information includes Supplemental Experimental Procedures, six figures, and four tables and can be found with this article online at https://doi.org/10.1016/j.celrep.2017.11.003.

AUTHOR CONTRIBUTIONS

C.L., O.G., B.B., M.B., L.A., M.A., P.D., A.M., and J.G. performed the biological experiments and sample preparation. M.A. and N.E. conducted data management. M.R., V.S., S.G., J.R., and F.P. performed the histochemical stainings and immunohistochemical scoring. V.M., O.T., M. Giovannini, M. Gasmi, M.O., J.E., E.B., A.G., J-L.R., P.G., M.B.-B., E.N., M. Gilabert, F.G., S.V., and J.-R.D. provided material. R.N., Y.B., and L.M. performed bioinformatics analysis. R.N., Y.B., L.M., G.L., J.-M.B., E.C., R.U., A.d.R., N.D., and J.I. contributed to the experimental design, data analysis and discussion. A.d.R., N.D., and J.I. directed the project. R.N., Y.B., L.M., N.D., and J.I. wrote the manuscript.

ACKNOWLEDGMENTS

This work is part of the national program Cartes d'Identité des Tumeurs (CIT) funded and developed by the Ligue Nationale Contre le Cancer. This work was supported by INCa, Cancéropôle PACA, Inserm and by DGOS through a SIRIC grant INCa-Inserm-DGOS 1068.

We thank Emilie Nouguerede, Jihane Pakradouni, Karim Sari, and Regis Vitestelle for their technical assistance and Aurélie Kamoun for fruitful discussions.

Received: July 3, 2017
Revised: September 12, 2017
Accepted: October 31, 2017
Published: November 28, 2017

REFERENCES

Bailey, P., Chang, D.K., Nones, K., Johns, A.L., Patch, A.-M., Gingras, M.-C., Miller, D.K., Christ, A.N., Bruxner, T.J.C., Quinn, M.C., et al.; Australian Pancreatic Cancer Genome Initiative (2016). Genomic analyses identify molecular subtypes of pancreatic cancer. Nature *531*, 47–52.

Barr, J., Vázquez-Chantada, M., Alonso, C., Pérez-Cormenzana, M., Mayo, R., Galán, A., Caballería, J., Martín-Duce, A., Tran, A., Wagner, C., et al. (2010). Liquid chromatography-mass spectrometry-based parallel metabolic profiling of human and mouse model serum reveals putative biomarkers associated

with the progression of nonalcoholic fatty liver disease. J. Proteome Res. *9*, 4501–4512.

Barr, J., Caballería, J., Martínez-Arranz, I., Domínguez-Díez, A., Alonso, C., Muntané, J., Pérez-Cormenzana, M., García-Monzón, C., Mayo, R., Martín-Duce, A., et al. (2012). Obesity-dependent metabolic signatures associated with nonalcoholic fatty liver disease progression. J. Proteome Res. *11*, 2521–2532.

Becht, E., Giraldo, N.A., Lacroix, L., Buttard, B., Elarouci, N., Petitprez, F., Selves, J., Laurent-Puig, P., Sautès-Fridman, C., Fridman, W.H., and de Reyniès, A. (2016). Estimating the population abundance of tissue-infiltrating immune and stromal cell populations using gene expression. Genome Biol. *17*, 218.

Bergmann, U., Funatomi, H., Yokoyama, M., Beger, H.G., and Korc, M. (1995). Insulin-like growth factor I overexpression in human pancreatic cancer: evidence for autocrine and paracrine roles. Cancer Res. *55*, 2007–2011.

Bradford, J.R., Farren, M., Powell, S.J., Runswick, S., Weston, S.L., Brown, H., Delpuech, O., Wappett, M., Smith, N.R., Carr, T.H., et al. (2013). RNA-seq differentiates tumour and host mRNA expression changes induced by treatment of human tumour xenografts with the VEGFR tyrosine kinase inhibitor cediranib. PLoS ONE *8*, e66003.

Cancer Genome Atlas Research Network. (2017). Integrated genomic characterization of pancreatic ductal adenocarcinoma. Cancer Cell *32*, 185–203.e13.

Carapuça, E.F., Gemenetzidis, E., Feig, C., Bapiro, T.E., Williams, M.D., Wilson, A.S., Delvecchio, F.R., Arumugam, P., Grose, R.P., Lemoine, N.R., et al. (2016). Anti-stromal treatment together with chemotherapy targets multiple signalling pathways in pancreatic adenocarcinoma. J. Pathol. *239*, 286–296.

Chen, H., Qin, S., Wang, M., Zhang, T., and Zhang, S. (2015). Association between cholesterol intake and pancreatic cancer risk: evidence from a meta-analysis. Sci. Rep. *5*, 8243.

Collisson, E.A., Sadanandam, A., Olson, P., Gibb, W.J., Truitt, M., Gu, S., Cooc, J., Weinkle, J., Kim, G.E., Jakkula, L., et al. (2011). Subtypes of pancreatic ductal adenocarcinoma and their differing responses to therapy. Nat. Med. *17*, 500–503.

Daemen, A., Peterson, D., Sahu, N., McCord, R., Du, X., Liu, B., Kowanetz, K., Hong, R., Moffat, J., Gao, M., et al. (2015). Metabolite profiling stratifies pancreatic ductal adenocarcinomas into subtypes with distinct sensitivities to metabolic inhibitors. Proc. Natl. Acad. Sci. USA *112*, E4410–E4417.

Farrow, B., Berger, D.H., and Rowley, D. (2009). Tumor-derived pancreatic stellate cells promote pancreatic cancer cell invasion through release of thrombospondin-2. J. Surg. Res. *156*, 155–160.

Gao, H., Korn, J.M., Ferretti, S., Monahan, J.E., Wang, Y., Singh, M., Zhang, C., Schnell, C., Yang, G., Zhang, Y., et al. (2015). High-throughput screening using patient-derived tumor xenografts to predict clinical trial drug response. Nat. Med. *21*, 1318–1325.

Guillaumond, F., Bidaut, G., Ouaissi, M., Servais, S., Gouirand, V., Olivares, O., Lac, S., Borge, L., Roques, J., Gayet, O., et al. (2015). Cholesterol uptake disruption, in association with chemotherapy, is a promising combined metabolic therapy for pancreatic adenocarcinoma. Proc. Natl. Acad. Sci. USA *112*, 2473–2478.

Guinney, J., Dienstmann, R., Wang, X., de Reyniès, A., Schlicker, A., Soneson, C., Marisa, L., Roepman, P., Nyamundanda, G., Angelino, P., et al. (2015). The consensus molecular subtypes of colorectal cancer. Nat. Med. *21*, 1350–1356.

Huang, B.Z., Chang, J.I., Li, E., Xiang, A.H., and Wu, B.U. (2016). Influence of statins and cholesterol on mortality among patients with pancreatic cancer. J. Natl. Cancer Inst. *109*, djw275.

Knudsen, E.S., Balaji, U., Mannakee, B., Vail, P., Eslinger, C., Moxom, C., Mansour, J., and Witkiewicz, A.K. (2017). Pancreatic cancer cell lines as patient-derived avatars: genetic characterisation and functional utility. Gut, Published January 10, 2017. https://doi.org/10.1136/gutjnl-2016-313133.

Lonardo, E., Hermann, P.C., Mueller, M.-T., Huber, S., Balic, A., Miranda-Lorenzo, I., Zagorac, S., Alcala, S., Rodriguez-Arabaolaza, I., Ramirez, J.C., et al. (2011). Nodal/Activin signaling drives self-renewal and tumorigenicity of pancreatic cancer stem cells and provides a target for combined drug therapy. Cell Stem Cell *9*, 433–446.

Marisa, L., de Reyniès, A., Duval, A., Selves, J., Gaub, M.P., Vescovo, L., Etienne-Grimaldi, M.-C., Schiappa, R., Guenot, D., Ayadi, M., et al. (2013). Gene expression classification of colon cancer into molecular subtypes: characterization, validation, and prognostic value. PLoS Med. *10*, e1001453.

Martínez-Arranz, I., Mayo, R., Pérez-Cormenzana, M., Mincholé, I., Salazar, L., Alonso, C., and Mato, J.M. (2015). Enhancing metabolomics research through data mining. J. Proteomics *127* (*Pt B*), 275–288.

Martinez-Garcia, R., Juan, D., Rausell, A., Muñoz, M., Baños, N., Menéndez, C., Lopez-Casas, P.P., Rico, D., Valencia, A., and Hidalgo, M. (2014). Transcriptional dissection of pancreatic tumors engrafted in mice. Genome Med. *6*, 27.

Moffitt, R.A., Marayati, R., Flate, E.L., Volmar, K.E., Loeza, S.G.H., Hoadley, K.A., Rashid, N.U., Williams, L.A., Eaton, S.C., Chung, A.H., et al. (2015). Virtual microdissection identifies distinct tumor- and stroma-specific subtypes of pancreatic ductal adenocarcinoma. Nat. Genet. *47*, 1168–1178.

Noll, E.M., Eisen, C., Stenzinger, A., Espinet, E., Muckenhuber, A., Klein, C., Vogel, V., Klaus, B., Nadler, W., Rösli, C., et al. (2016). CYP3A5 mediates basal and acquired therapy resistance in different subtypes of pancreatic ductal adenocarcinoma. Nat. Med. *22*, 278–287.

Nones, K., Waddell, N., Song, S., Patch, A.-M., Miller, D., Johns, A., Wu, J., Kassahn, K.S., Wood, D., Bailey, P., et al.; APGI (2014). Genome-wide DNA methylation patterns in pancreatic ductal adenocarcinoma reveal epigenetic deregulation of SLIT-ROBO, ITGA2 and MET signaling. Int. J. Cancer *135*, 1110–1118.

Ohnishi, N., Miyata, T., Ohnishi, H., Yasuda, H., Tamada, K., Ueda, N., Mashima, H., and Sugano, K. (2003). Activin A is an autocrine activator of rat pancreatic stellate cells: potential therapeutic role of follistatin for pancreatic fibrosis. Gut *52*, 1487–1493.

Olive, K.P., Jacobetz, M.A., Davidson, C.J., Gopinathan, A., McIntyre, D., Honess, D., Madhu, B., Goldgraben, M.A., Caldwell, M.E., Allard, D., et al. (2009). Inhibition of Hedgehog signaling enhances delivery of chemotherapy in a mouse model of pancreatic cancer. Science *324*, 1457–1461.

Pan, C.-X., Zhang, H., Tepper, C.G., Lin, T.-Y., Davis, R.R., Keck, J., Ghosh, P.M., Gill, P., Airhart, S., Bult, C., et al. (2015). Development and characterization of bladder cancer patient-derived xenografts for molecularly guided targeted therapy. PLoS ONE *10*, e0134346.

Qian, L.-W., Mizumoto, K., Maehara, N., Ohuchida, K., Inadome, N., Saimura, M., Nagai, E., Matsumoto, K., Nakamura, T., and Tanaka, M. (2003). Co-cultivation of pancreatic cancer cells with orthotopic tumor-derived fibroblasts: fibroblasts stimulate tumor cell invasion via HGF secretion whereas cancer cells exert a minor regulative effect on fibroblasts HGF production. Cancer Lett. *190*, 105–112.

Rhim, A.D., Oberstein, P.E., Thomas, D.H., Mirek, E.T., Palermo, C.F., Sastra, S.A., Dekleva, E.N., Saunders, T., Becerra, C.P., Tattersall, I.W., et al. (2014). Stromal elements act to restrain, rather than support, pancreatic ductal adenocarcinoma. Cancer Cell *25*, 735–747.

Secq, V., Leca, J., Bressy, C., Guillaumond, F., Skrobuk, P., Nigri, J., Lac, S., Lavaut, M.-N., Bui, T.-T., Thakur, A.K., et al. (2015). Stromal SLIT2 impacts on pancreatic cancer-associated neural remodeling. Cell Death Dis. *6*, e1592.

Sherman, M.H., Yu, R.T., Engle, D.D., Ding, N., Atkins, A.R., Tiriac, H., Collisson, E.A., Connor, F., Van Dyke, T., Kozlov, S., et al. (2014). Vitamin D receptor-mediated stromal reprogramming suppresses pancreatitis and enhances pancreatic cancer therapy. Cell *159*, 80–93.

Song, H.-N., Lee, C., Kim, S.T., Kim, S.Y., Kim, N.K.D., Jang, J., Kang, M., Jang, H., Ahn, S., Kim, S.H., et al. (2016). Molecular characterization of colorectal cancer patients and concomitant patient-derived tumor cell establishment. Oncotarget *7*, 19610–19619.

Tape, C.J., Ling, S., Dimitriadi, M., McMahon, K.M., Worboys, J.D., Leong, H.S., Norrie, I.C., Miller, C.J., Poulogiannis, G., Lauffenburger, D.A., and Jørgensen, C. (2016). Oncogenic KRAS regulates tumor cell signaling via stromal reciprocation. Cell *165*, 910–920.

Tian, H., Callahan, C.A., DuPree, K.J., Darbonne, W.C., Ahn, C.P., Scales, S.J., and de Sauvage, F.J. (2009). Hedgehog signaling is restricted to the stromal compartment during pancreatic carcinogenesis. Proc. Natl. Acad. Sci. USA *106*, 4254–4259.

Topalovski, M., and Brekken, R.A. (2016). Matrix control of pancreatic cancer: new insights into fibronectin signaling. Cancer Lett. *381*, 252–258.

Townsend, E.C., Murakami, M.A., Christodoulou, A., Christie, A.L., Köster, J., DeSouza, T.A., Morgan, E.A., Kallgren, S.P., Liu, H., Wu, S.-C., et al. (2016). The public repository of xenografts enables discovery and randomized phase II-like trials in mice. Cancer Cell *29*, 574–586.

Ueki, T., Toyota, M., Sohn, T., Yeo, C.J., Issa, J.P., Hruban, R.H., and Goggins, M. (2000). Hypermethylation of multiple genes in pancreatic adenocarcinoma. Cancer Res. *60*, 1835–1839.

Walker, E.J., Ko, A.H., Holly, E.A., and Bracci, P.M. (2015). Statin use and risk of pancreatic cancer: results from a large, clinic-based case-control study. Cancer *121*, 1287–1294.

Whatcott, C., Han, H., Posner, R.G., and Von Hoff, D.D. (2013). Tumor-stromal interactions in pancreatic cancer. Crit. Rev. Oncog. *18*, 135–151.

Witkiewicz, A.K., McMillan, E.A., Balaji, U., Baek, G., Lin, W.-C., Mansour, J., Mollaee, M., Wagner, K.-U., Koduru, P., Yopp, A., et al. (2015). Whole-exome sequencing of pancreatic cancer defines genetic diversity and therapeutic targets. Nat. Commun. *6*, 6744.

Witkiewicz, A.K., Balaji, U., Eslinger, C., McMillan, E., Conway, W., Posner, B., Mills, G.B., O'Reilly, E.M., and Knudsen, E.S. (2016). Integrated patient-derived models delineate individualized therapeutic vulnerabilities of pancreatic cancer. Cell Rep. *16*, 2017–2031.

Wu, B.U., Chang, J., Jeon, C.Y., Pandol, S.J., Huang, B., Ngor, E.W., Difronzo, A.L., and Cooper, R.M. (2015). Impact of statin use on survival in patients undergoing resection for early-stage pancreatic cancer. Am. J. Gastroenterol. *110*, 1233–1239.

Cell Reports, Volume *21*

Supplemental Information

Pancreatic Adenocarcinoma Therapeutic Targets Revealed by Tumor-Stroma Cross-Talk Analyses in Patient-Derived Xenografts

Rémy Nicolle, Yuna Blum, Laetitia Marisa, Celine Loncle, Odile Gayet, Vincent Moutardier, Olivier Turrini, Marc Giovannini, Benjamin Bian, Martin Bigonnet, Marion Rubis, Nabila Elarouci, Lucile Armenoult, Mira Ayadi, Pauline Duconseil, Mohamed Gasmi, Mehdi Ouaissi, Aurélie Maignan, Gwen Lomberk, Jean-Marie Boher, Jacques Ewald, Erwan Bories, Jonathan Garnier, Anthony Goncalves, Flora Poizat, Jean-Luc Raoul, Veronique Secq, Stephane Garcia, Philippe Grandval, Marine Barraud-Blanc, Emmanuelle Norguet, Marine Gilabert, Jean-Robert Delpero, Julie Roques, Ezequiel Calvo, Fabienne Guillaumond, Sophie Vasseur, Raul Urrutia, Aurélien de Reyniès, Nelson Dusetti, and Juan Iovanna

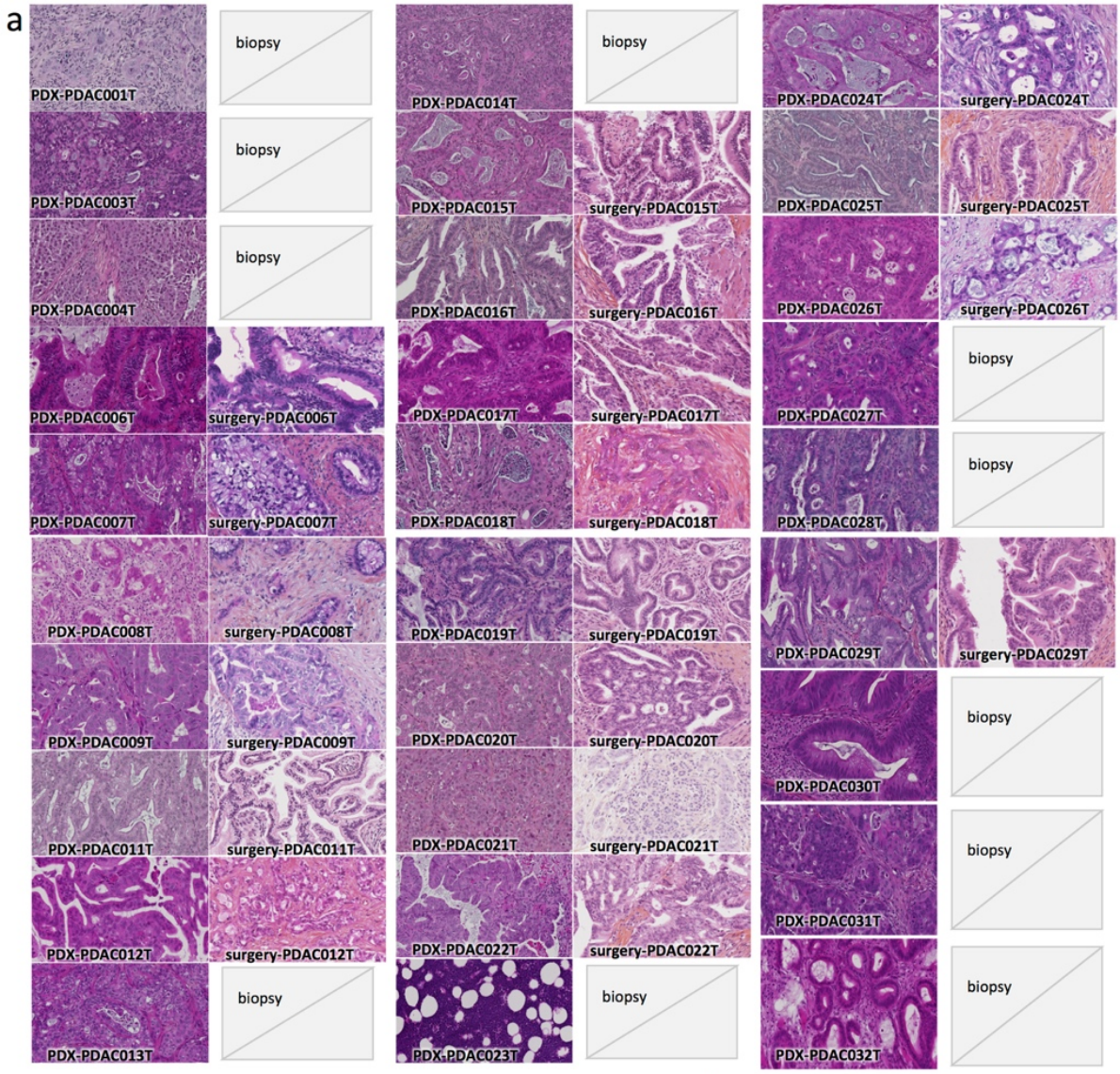
a
PDX-PDAC001T
biopsy
PDX-PDAC003T
biopsy
PDX-PDAC004T
biopsy
PDX-PDAC006T
surgery-PDAC006T
PDX-PDAC007T
surgery-PDAC007T
PDX-PDAC008T
surgery-PDAC008T
PDX-PDAC009T
surgery-PDAC009T
PDX-PDAC011T
surgery-PDAC011T
PDX-PDAC012T
surgery-PDAC012T
PDX-PDAC013T
biopsy
PDX-PDAC014T
biopsy
PDX-PDAC015T
surgery-PDAC015T
PDX-PDAC016T
surgery-PDAC016T
PDX-PDAC017T
surgery-PDAC017T
PDX-PDAC018T
surgery-PDAC018T
PDX-PDAC019T
surgery-PDAC019T
PDX-PDAC020T
surgery-PDAC020T
PDX-PDAC021T
surgery-PDAC021T
PDX-PDAC022T
surgery-PDAC022T
PDX-PDAC023T
biopsy
PDX-PDAC024T
surgery-PDAC024T
PDX-PDAC025T
surgery-PDAC025T
PDX-PDAC026T
surgery-PDAC026T
PDX-PDAC027T
biopsy
PDX-PDAC028T
biopsy
PDX-PDAC029T
surgery-PDAC029T
PDX-PDAC030T
biopsy
PDX-PDAC031T
biopsy
PDX-PDAC032T
biopsy

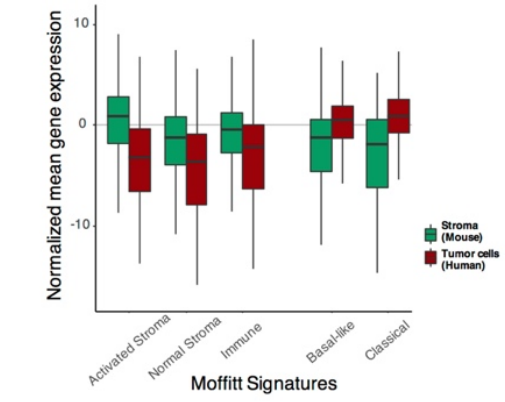
b
Normalized mean gene expression
10
0
-10
Stroma (Mouse)
Tumor cells (Human)
Activated Stroma
Normal Stroma
Immune
Basal-like
Classical
Moffitt Signatures

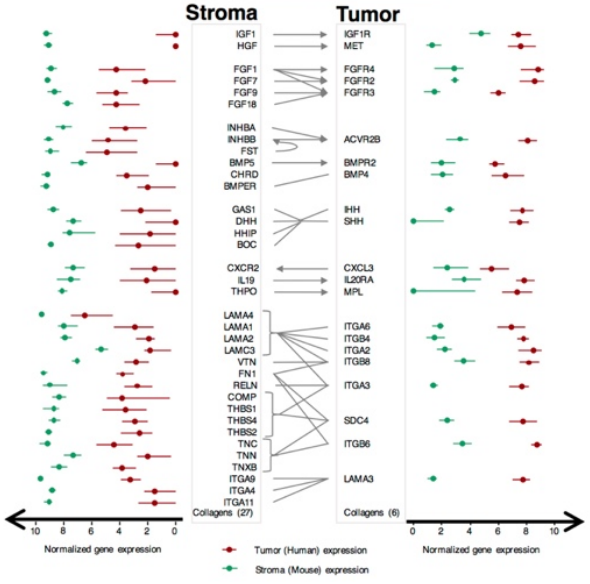
c
Stroma
Tumor
IGF1
HGF
IGF1R
MET
FGF1
FGF7
FGF9
FGF18
FGFR4
FGFR2
FGFR3
INHBA
INHBB
FST
BMP5
CHRD
BMPER
ACVR2B
BMPR2
BMP4
GAS1
DHH
HHIP
BOC
IHH
SHH
CXCR2
IL19
THPO
CXCL3
IL2RA
MPL
LAMA4
LAMA1
LAMA2
LAMC3
VTN
FN1
RELN
COMP
THBS1
THBS4
THBS2
TNC
TNN
TNXB
ITGA9
ITGA4
ITGA11
Collagens (27)
ITGA6
ITGB4
ITGA2
ITGB8
ITGA3
SDC4
ITGB6
LAMA3
Collagens (6)
Normalized gene expression
Tumor (Human) expression
Stroma (Mouse) expression
Normalized gene expression

Figure S1. PDX stromal analysis. Related to figure 1. a. Hematoxylin and eosin staining of PDX tumor and original human primary resected tumors. **b**. Distribution of expression (normalized FPKM) of the gene signatures by Moffitt et al. in the tumor (red) and the stroma (green). Expression data were normalized to allow comparison between human and mouse RNAseq quantification. **c**. Tumor (red) and stromal (green) expression of genes in pathways potentially involved in tumor/stroma cross talk. Values shown are median expressions and error bars indicate first and third quartiles. Expression data were normalized to allow comparison between human and mouse RNAseq quantification and gene-wise scaled.

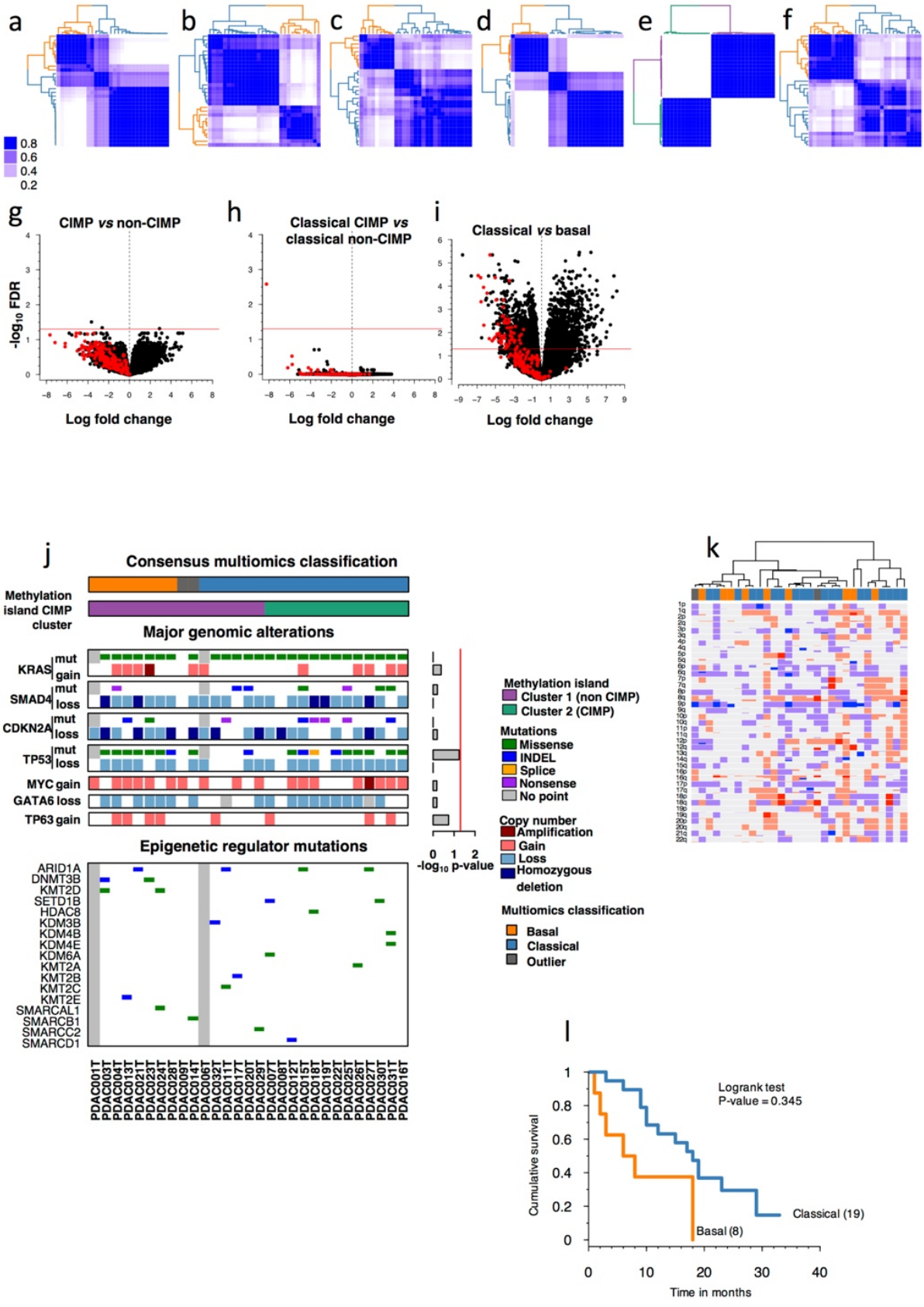
a
b
c
d
e
f
0.8
0.6
0.4
0.2
g
CIMP vs non-CIMP
-log10 FDR
Log fold change
h
Classical CIMP vs classical non-CIMP
Log fold change
i
Classical vs basal
Log fold change
j
Consensus multiomics classification
Methylation island CIMP cluster
Major genomic alterations
KRAS mut gain
SMAD4 mut loss
CDKN2A mut loss
TP53 mut loss
MYC gain
GATA6 loss
TP63 gain
Epigenetic regulator mutations
ARID1A
DNMT3B
KMT2D
SETD1B
HDAC8
KDM3B
KDM4B
KDM4E
KDM6A
KMT2A
KMT2B
KMT2C
KMT2E
SMARCAL1
SMARCB1
SMARCC2
SMARCD1
PDAC001T PDAC003T PDAC004T PDAC013T PDAC021T PDAC023T PDAC024T PDAC028T PDAC009T PDAC014T PDAC006T PDAC032T PDAC011T PDAC017T PDAC020T PDAC029T PDAC007T PDAC012T PDAC015T PDAC018T PDAC022T PDAC025T PDAC026T PDAC027T PDAC030T PDAC031T PDAC016T
0 1 2
-log10 p-value
Methylation island
Cluster 1 (non CIMP)
Cluster 2 (CIMP)
Mutations
Missense
INDEL
Splice
Nonsense
No point
Copy number
Amplification
Gain
Loss
Homozygous deletion
Multiomics classification
Basal
Classical
Outlier
k
l
Logrank test
P-value = 0.345
Cumulative survival
Classical (19)
Basal (8)
Time in months

Figure S2. Multi-omics classifications. Related to figure 2. Co-occurrence heatmaps of the consensus clustering applied to protein coding mRNA (**a**), long non-coding RNA (**b**), microRNA (**c**), non-CpG island methylation (**d**), CpG island methylation (**e**) and to mouse/stromal mRNA (f). Value represented range from 0 (never co-clustered in any bootstrap iteration) to 1 (always co-clustered). **g**. Volcano plot of differential tumor gene expression between CIMP and non-CIMP samples. Y-axis: $-\log_{10}$ limma-voom FDR adjusted p-value. **h**. Volcano plot of differential tumor gene expression between classical CIMP and classical non-CIMP samples. Y-axis: $-\log_{10}$ limma-voom FDR adjusted p-value. **i**. Volcano plot of differential tumor gene expression between basal and classical samples. Y-axis: $-\log_{10}$ limma-voom FDR adjusted p-value. Red points indicate genes that are significantly negatively correlated (Pearson's correlation, FDR 5%) to CpG that are significantly hypermethylated (t-test, FDR 5%) in CIMP samples and are reported in supplementary table 2. **j**. Most frequent genomic alterations, including point mutations (mut) and copy number aberrations. **k**. Consensus classification of Copy Number Aberrations using SNP chips. Heatmap shows the most variant copy number status of each chromosome arm. **l**. Kaplan-Meier plot of survival in two subtypes. The logrank test p-value shown was done after correcting for curative surgery. Basal median survival: 7 months, Classical median survival: 18 months.

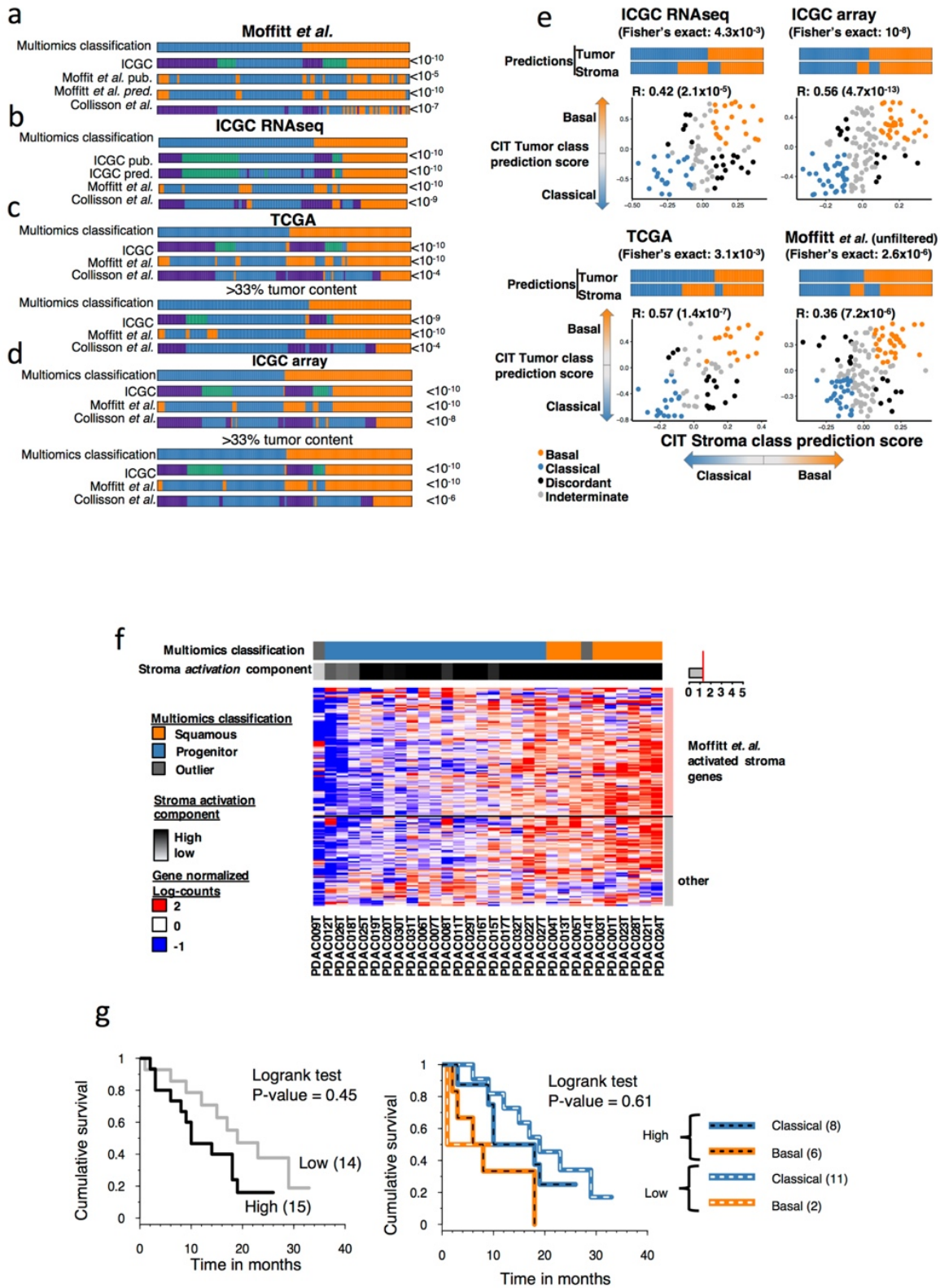
a
Moffitt et al.
Multiomics classification
ICGC
Moffit et al. pub.
Moffitt et al. pred.
Collisson et al.
b
ICGC RNAseq
Multiomics classification
ICGC pub.
ICGC pred.
Moffitt et al.
Collisson et al.
c
TCGA
Multiomics classification
ICGC
Moffitt et al.
Collisson et al.
>33% tumor content
d
ICGC array
e
ICGC RNAseq
(Fisher's exact: 4.3x10-3)
ICGC array
(Fisher's exact: 10-8)
Predictions
Tumor
Stroma
R: 0.42 (2.1x10-5)
R: 0.56 (4.7x10-13)
Basal
CIT Tumor class prediction score
Classical
TCGA
(Fisher's exact: 3.1x10-3)
Moffitt et al. (unfiltered)
(Fisher's exact: 2.6x10-6)
R: 0.57 (1.4x10-7)
R: 0.36 (7.2x10-6)
CIT Stroma class prediction score
Basal
Classical
Discordant
Indeterminate
f
Multiomics classification
Stroma activation component
Squamous
Progenitor
Outlier
High
low
Gene normalized Log-counts
Moffitt et. al. activated stroma genes
other
g
Logrank test
P-value = 0.45
Low (14)
High (15)
Cumulative survival
Time in months
Logrank test
P-value = 0.61
High
Low
Classical (8)
Basal (6)
Classical (11)
Basal (2)

Figure S3. Stromal classification of PDAC. Related to figure 2. PDAC classifications applied to public expression datasets. Classifiers were trained on their original datasets and applied to public expression datasets: Moffitt *et al.*[1] (**a**) from the RNAseq dataset of the ICGC[2] (**b**), the expression array data from the ICGC[2] (**c**, upper panel all samples, lower panel samples filtered based on tumor cell purity) and the TCGA (**d**, upper panel all samples, lower panel samples filtered based on tumor cell purity). P-values of a Chi2 test of independence between each classification and the predictions of the PDX-based classified (Multiomics classification). When a classification is given in the original publication it is noted as *pub.* while the prediction of the classifier trained on the same dataset to be applied to others is noted as *pred.* **e.** Application of the PDX-based tumor and stromal predictors on human primary PDAC transcriptome datasets. For each dataset, the subtype predictions (heatmap, upper panels) and the prediction scores (scatter plot, lower panel) are shown. Prediction heatmap panels exclude low confident predictions shown as indeterminate points (grey) in lower panels. Scatter plot axes represent tumor (y-axis) and stroma (x-axis) subtype prediction scores for which positive scores corresponds to the basal subtype and negative scores to the classical subtype. ICGC RNAseq, ICGC array and TCGA contain only samples with at least 33% of estimated tumor cell content. Fisher's exact test were computed without indeterminate samples. R: Pearson's correlation including indeterminate samples. **f**. Sample projection on the stroma activation component and expression of the top contributing stromal genes. Lateral bar represents the $-\log_{10}$ transformed p-value of a one-way ANOVA. Rows in the heatmap indicate genes that were found in the *activated stroma* component described by Moffitt *et al.* (pink) and genes that were either found in other components or not found in the analysis (*e.g.* no known human homolog genes). **g**. Kaplan-Meier plot of survival of samples projected above (high) or below (low) median sample projection on the stromal activation component (left panel) and in combination with tumor classification (right panel). The logrank test p-value shown was done after correcting for curative surgery.

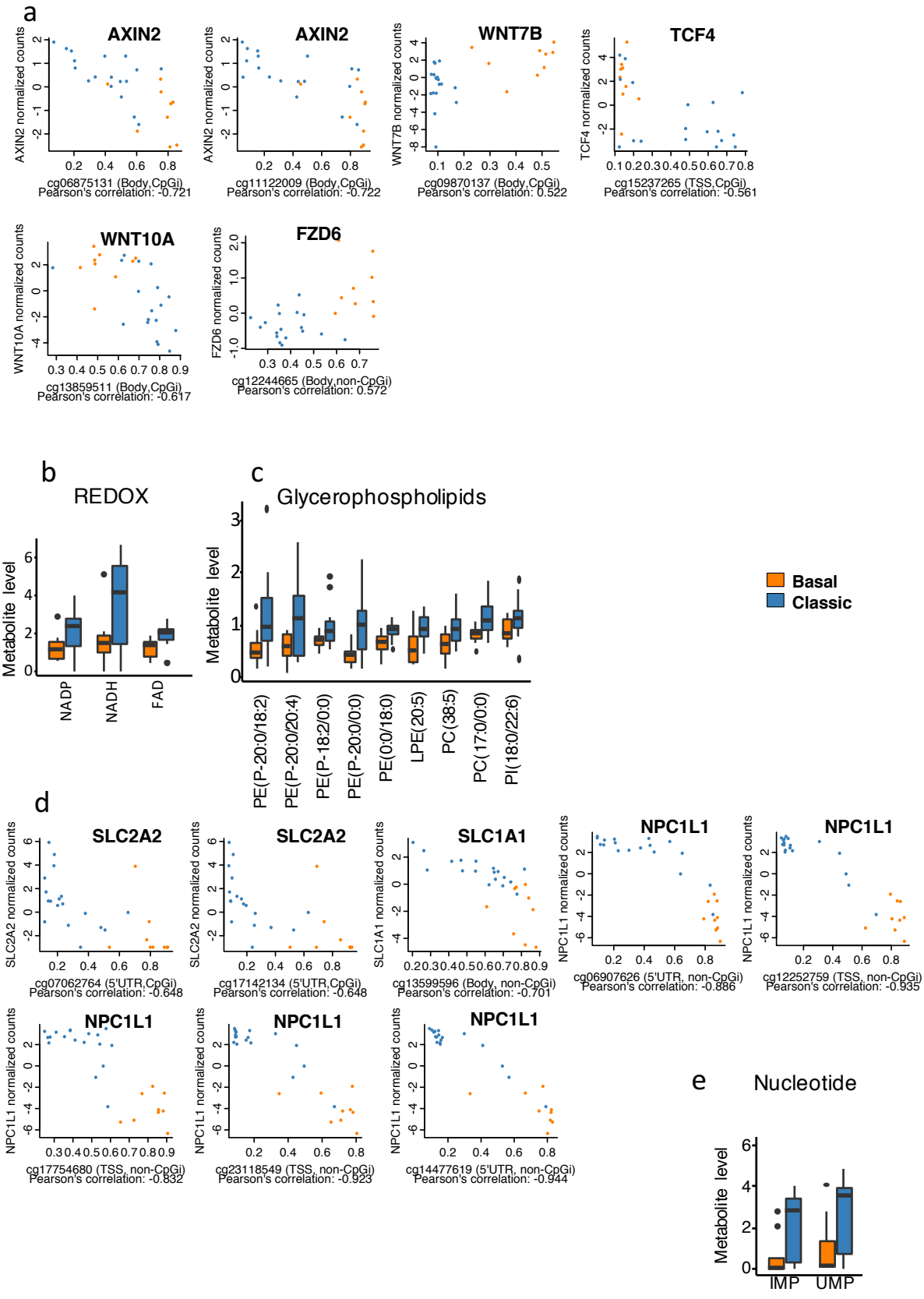
a
AXIN2
AXIN2 normalized counts
cg06875131 (Body,CpGi)
Pearson's correlation: -0.721
AXIN2
AXIN2 normalized counts
cg11122009 (Body,CpGi)
Pearson's correlation: -0.722
WNT7B
WNT7B normalized counts
cg09870137 (Body,CpGi)
Pearson's correlation: 0.522
TCF4
TCF4 normalized counts
cg15237265 (TSS,CpGi)
Pearson's correlation: -0.561
WNT10A
WNT10A normalized counts
cg13859511 (Body,CpGi)
Pearson's correlation: -0.617
FZD6
FZD6 normalized counts
cg12244665 (Body,non-CpGi)
Pearson's correlation: 0.572
b
REDOX
Metabolite level
NADP
NADH
FAD
c
Glycerophospholipids
Metabolite level
PE(P-20:0/18:2)
PE(P-20:0/20:4)
PE(P-18:2/0:0)
PE(P-20:0/0:0)
PE(0:0/18:0)
LPE(20:5)
PC(38:5)
PC(17:0/0:0)
PI(18:0/22:6)
Basal
Classic
d
SLC2A2
SLC2A2 normalized counts
cg07062764 (5'UTR,CpGi)
Pearson's correlation: -0.648
SLC2A2
SLC2A2 normalized counts
cg17142134 (5'UTR,CpGi)
Pearson's correlation: -0.648
SLC1A1
SLC1A1 normalized counts
cg13599596 (Body, non-CpGi)
Pearson's correlation: -0.701
NPC1L1
NPC1L1 normalized counts
cg06907626 (5'UTR, non-CpGi)
Pearson's correlation: -0.886
NPC1L1
NPC1L1 normalized counts
cg12252759 (TSS, non-CpGi)
Pearson's correlation: -0.935
NPC1L1
NPC1L1 normalized counts
cg17754680 (TSS, non-CpGi)
Pearson's correlation: -0.832
NPC1L1
NPC1L1 normalized counts
cg23118549 (TSS, non-CpGi)
Pearson's correlation: -0.923
NPC1L1
NPC1L1 normalized counts
cg14477619 (5'UTR, non-CpGi)
Pearson's correlation: -0.944
e
Nucleotide
Metabolite level
IMP
UMP

Figure S4. Epigenetic and metabolic characterization of PDAC subtypes. Related to figures 3, 4 and 5. a. Scatter plots of the expression and methylation value of the genes and their associated CpG shown in figure 3. Gene expression are normalized log counts after gene-wise centering. Methylation levels are normalized Beta-values. **b**. Metabolomic comparison of basal and classical tumors of **b**. REDOX metabolites. **c**. Glycerophospholipides. PE: phosphoethanolamine ; LPE: lysophsphatidylethanolamine ; PC: phosphocholine ; PI: phosphoinositol. **d.** Scatter plots of the expression and methylation value of the genes and their associated CpG shown in figure 5. Gene expression are normalized log counts after gene-wise centering. Methylation levels are normalized Beta-values. **e.** Metabolomic comparison of basal and classical tumors of Nucleotides. IMP: inosine mono-phosphate ; UMP: Uridine mono-phosphate. All metabolites shown are differential between the two subtypes (Student's t test, alpha=0.05).

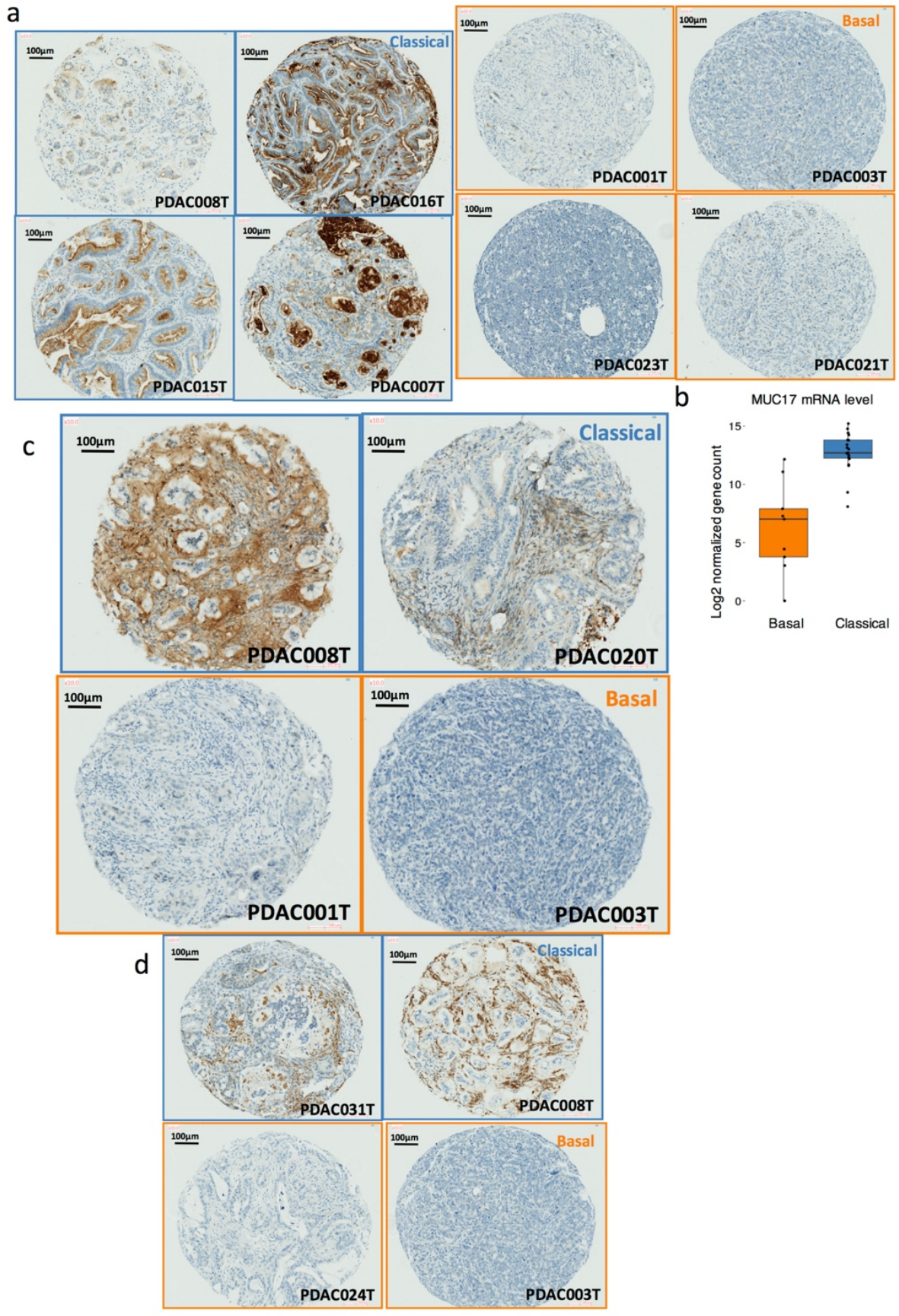
a
100µm
PDAC008T
Classical
PDAC016T
PDAC015T
PDAC007T
Basal
PDAC001T
PDAC003T
PDAC023T
PDAC021T
b
MUC17 mRNA level
Log2 normalized gene count
15
10
5
0
Basal
Classical
c
PDAC008T
Classical
PDAC020T
PDAC001T
Basal
PDAC003T
d
PDAC031T
Classical
PDAC008T
PDAC024T
Basal
PDAC003T

Figure S5. Subtype-specific tumor and stromal immunohistochemistry. Related to figures 4 and 5. a. Immunohistochemical staining of MUC17 in classical (upper panels) and basal (lower panels) PDX samples. **b**. Boxplot of the expression level of MUC17 human mRNA in basal and classical PDX samples. No detectable level of the murine MUC17 mRNA. Immunohistochemical staining of PPARG **c.** and **d.** FABP5 in PDX samples.

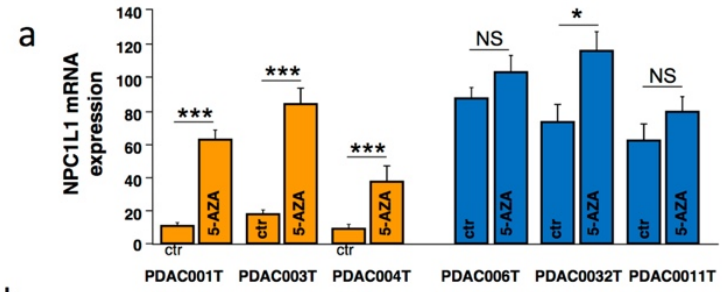
a
NPC1L1 mRNA expression
140
120
100
80
60
40
20
0
***
***
***
NS
*
NS
ctr
5-AZA
PDAC001T
PDAC003T
PDAC004T
PDAC006T
PDAC0032T
PDAC0011T

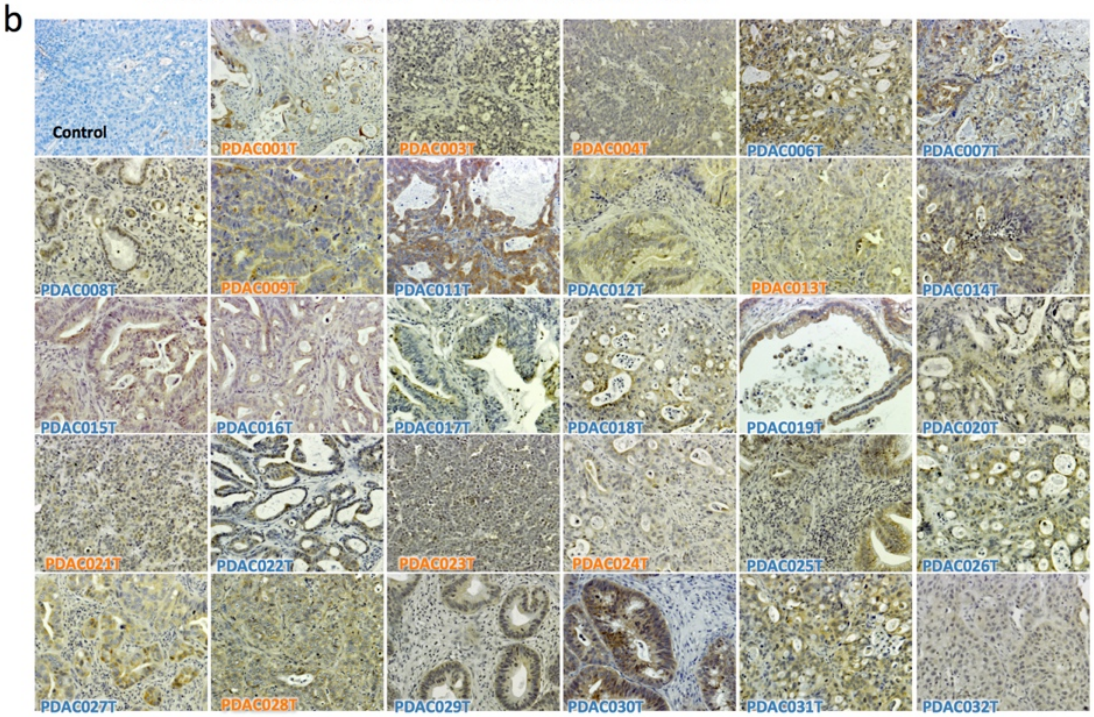
b
Control
PDAC001T
PDAC003T
PDAC004T
PDAC006T
PDAC007T
PDAC008T
PDAC009T
PDAC011T
PDAC012T
PDAC013T
PDAC014T
PDAC015T
PDAC016T
PDAC017T
PDAC018T
PDAC019T
PDAC020T
PDAC021T
PDAC022T
PDAC023T
PDAC024T
PDAC025T
PDAC026T
PDAC027T
PDAC028T
PDAC029T
PDAC030T
PDAC031T
PDAC032T

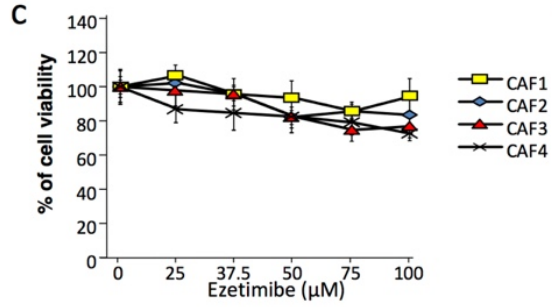
c
% of cell viability
140
120
100
80
60
40
20
0
0
25
37.5
50
75
100
Ezetimibe (μM)
CAF1
CAF2
CAF3
CAF4

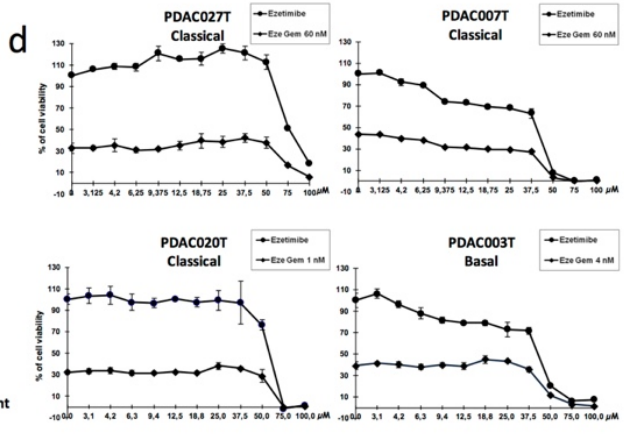
d
PDAC027T
Classical
PDAC007T
Classical
PDAC020T
Classical
PDAC003T
Basal
Ezetimibe
Eze Gem 60 nM
Eze Gem 1 nM
Eze Gem 4 nM
% of cell viability

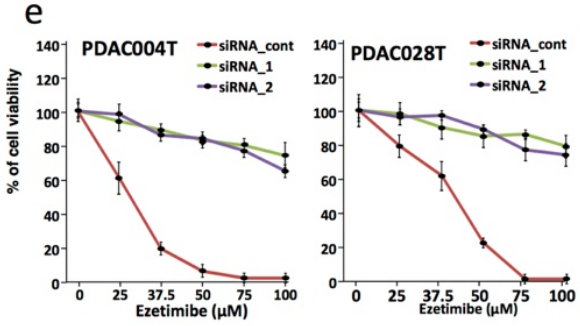
e
PDAC004T
PDAC028T
siRNA_cont
siRNA_1
siRNA_2
% of cell viability
Ezetimibe (μM)

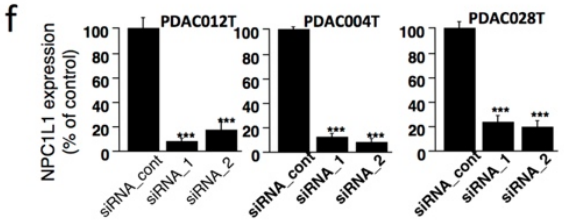
f
PDAC012T
PDAC004T
PDAC028T
NPC1L1 expression (% of control)
siRNA_cont
siRNA_1
siRNA_2
***

Figure S6. NPC1L1 therapeutic targeting validation. Related to figure 6. a. NPC1L1 expression after demethylating treatment using 5-aza-2'-deoxycytidine. The mRNA level of NPC1L1 was measured by quantitative RT-PCR in Pancreatic ductal adenocarcinoma–derived cells with or without 5-aza-2'-deoxycytidine (respectively ctr and 5-AZA). Each experiment was done in triplicate. Error bars represent standard deviation. **b.** NPC1L1 immunostaining in the PDX cohort. **c**. Effect Ezetimib treatment on cancer associated fibroblasts. Ezetimibe sensitivity of 4 human cancer associated fibroblasts. Dose-response curves after 72h of Ezetimibe treatment. Cell viability is indicated in % to the control (vehicle treated). Error bars represent SEM; n = 6. **d**. Chemograms with Ezetimibe alone or associated with Gemcitabine. Pancreatic ductal adenocarcinoma–derived cells were treated with increasing concentrations of Ezetimibe alone or associated with 3 fixed different concentrations of Gemcitabine (60 nM, 4nM or 1 nM). The concentration of Gemcitabine was chosen to induce a mortality ranging from 30 to 70% (DL30 to 70). The percentage of cell viability was measured after 72 hours of treatment. A sensitivity profile was obtained for each drug. Each experiment was done in triplicate and repeated 3 times with similar results. Error bars represent standard deviation. **e**. Dose-response curves in two Pancreatic ductal adenocarcinoma–derived cells after 72h of Ezetimibe treatment with NPC1L1 siRNA knockdown or a control siRNA. Cell viability is indicated in % to the control (vehicle treated). Error bars represent SEM; n = 6. **f**. Validation of NPC1L1-directed siRNA on gene expression (triplicates).

Extended experimental procedure

SUPPLEMENTARY EXPERIMENTAL PROCEDURES

Patient-derived xenograft

Three expert clinical centers collaborated on this project after receiving ethics review board approval. Patients were included in this project under the Paoli-Calmettes Institute clinical trial number 2011-A01439-32. Consent forms of informed patients were collected and registered in a central database. The tumor tissues used for xenograft generation were deemed excess to that required for the patient's diagnosis.

PDAC tissue from surgical samples was fragmented, mixed with 100 µL of Matrigel and implanted with a trocar (10 gauge; Innovative Research of America, Sarasota, FL) in the subcutaneous right upper flank of an anesthetized and disinfected male NMRI-nude mouse.

Samples obtained from EUS-FNA were mixed with 100 µL of Matrigel (BD Biosciences, Franklin Lakes, NJ) and injected in the upper right flank of a male nude mice (Swiss Nude Mouse Crl: NU(lco)-Foxn1nu; Charles River Laboratories, Wilmington, MA) for the first implantation. When xenografts reached 1 cm^3, these were removed and passed to NMRI-nude mice in the same manner than surgical samples.

All animal experiments were conducted in accordance with institutional guidelines and were approved by the "Plateforme de Stabulation et d'Expérimentation Animale" (PSEA, Scientific Park of Luminy, Marseille).

DNA and RNA extraction

Nucleic acids were extracted for 30 xenografts samples corresponding to 29 unique patients. DNA was extracted using Blood & Cell culture DNA mini kit (Qiagen) following the manufacturer's instructions. RNA were extracted using trizol and Guanidine Isothiocyanate and isolated with the miRneasy Mini kit (Qiagen) as previously described [4].

Whole-exome sequencing and analysis

Exome sequencing was performed in 27 pairs of PDX and matched normal samples (from blood). Library preparation, exome capture and sequencing have been done by IntegraGen SA (Evry, France). Genomic DNA was captured using Agilent in-solution enrichment methodology (SureSelect XT Human All Exon V5-UTR, Agilent) with their biotinylated oligonucleotides probes library (SureSelect XT Human All Exon V5-UTR - 70 Mb, Agilent), followed by paired-end 75 bases massively parallel sequencing on Illumina HiSeq2500. Sequence capture, enrichment and elution were performed according to

manufacturer's instruction and protocols (SureSelect, Agilent) without modification except for library preparation performed with NEBNext® Ultra kit (New England Biolabs®). Image analysis and base calling was performed using Illumina Real Time Analysis (2.7.3) with default parameters. Reads were mapped and processed using BWA-MEM [5] and SMAP on the human hg19 and mouse mm38 genomes (Ensembl 75). The human mapped reads were processed using GATK [6] based on the Mutect2 exome somatic calling best practice pipeline [7,8]. Mutations were annotated using ANNOVAR [9].
Genotype data has been deposited at the European Genome-phenome Archive (EGA, http://www.ebi.ac.uk/ega/), which is hosted by the EBI, under accession number EGAS00001001928.

SNP arrays analysis

Illumina Infinium HumanCode-24 BeadChip SNP arrays were used to analyze the DNA samples. Integragen SA (Evry, France) carried out hybridization, according to the manufacturer's recommendations. The BeadStudio software (Illumina) was used to normalize raw fluorescent signals and to obtain log R ratio (LRR) and B allele frequency (BAF) values. Asymmetry in BAF signals due to bias between the two dyes used in Illumina assays was corrected using the tQN normalization procedure [10]. We used the circular binary segmentation algorithm [11] to segment genomic profiles and assign corresponding smoothed values of log R ratio and B allele frequency. The Genome Alteration Print (GAP) method was used to determine the ploidy of each sample, the level of contamination with normal cells and the allele-specific copy number of each segment [12]. Chromosomal instability index (CIN) was estimated by the mean number of SNP probes with a loss or gained status normalized by chromosomes length. SNP data is available through ArrayExpress (http://www.ebi.ac.uk/arrayexpress) under accession E-MTAB-5006.

DNA methylation profiling and analysis

Whole-genome DNA methylation was analyzed using the Illumina Infinium HumanMethylation450 Beadchip. Integragen SA (Evry, France) carried out microarray experiments and hybridized to the BeadChip arrays following the manufacturer's instructions. Illumina GenomeStudio software was used to extract the Beta-value DNA methylation score for each locus. We removed data from probes that contained SNPs or overlapped with a repetitive element that was not uniquely aligned to the human genome or regions of insertions and deletions in the human genome.
The CpG Island Methylator Phenotype (CIMP) index was determined using methylation Illumina Infinium HumanMethylation450 BeadChip based on previous low throughput work [13]. In brief, all island CpG found to be unmethylated (<20% Beta-value) in all 25 normal pancreatic samples from the ICGC consortium [14] were selected. The CIMP index

was calculated independently for each sample as the proportion of methylated (>30% Beta-value) CpGs among the selected normally unmethylated island CpG.
Methylation data is available through ArrayExpress (http://www.ebi.ac.uk/arrayexpress) under accession E-MTAB-5008.

microRNA profiling and analysis

Total RNAs are purified with miRNeasy kit which allows the selection of the small RNA fraction less than 100b. From these samples enriched in small RNAs, libraries are performed according to previously established protocols [15]. After the sequencing platform generates the sequencing images, the data are analyzed in three steps: image analysis, base calling and bcl conversion. CASAVA demultiplexes multiplexed samples during the bcl conversion step. Convert *bcl files into compressed FASTQ files. To do some quality control checks on raw sequence data, fastqc software is used. Finally, the script "Trim_adapter", provides by mirExpress software, handles the sequence file which contain adapter or not according the input of adaptor sequence. The sequence adapter was trimmed on sequence data.
sRNAbench [16] software (version 10/14) was used to quantify read counts for each human and mouse miRNA referenced in mirBase21. One sample (PDAC016T) was removed following quality check. Only mature miRNA with at least three read counts in at least 3 samples were kept for further analysis. Gene counts were normalized using the upper-quartile approach [17]. miRNA sequencing data is available through ArrayExpress (http://www.ebi.ac.uk/arrayexpress) under accession E-MTAB-5018.

mRNA profiling and analysis

mRNA profiles were obtained using Illumina's TrueSeq Stranded mRNA LT protocol. Sequencing followed oligo-dT capture and was done on a paired-end 100 pair flow cell. mRNA libraries were prepared and sequenced by AROS Applied Biotechnology A/S (Aarhus, Denmark). RNAseq reads were mapped using STAR [18] with the proposed ENCODE parameters) and SMAP on the human hg19 and mouse mmu38 genomes and transcript annotation (Ensembl 75). Gene expression profiles were obtained using FeatureCount [19]. Only genes with at least three read counts in at least 3 samples were kept for further analysis. Gene counts were normalized using the upper-quartile approach [17].
When specified, the expression of protein coding mRNA corresponds to the selection of genes annotated in Ensembl as protein coding while the long non-coding RNA annotation was taken from Carlevaro-Fita and colleagues work [20].
Immune cell population estimation was done by applying MCP-counter [21] on the stromal expression dataset.
The direct comparison between human and mouse based gene counts was done on the subset of unique homolog gene pairs (downloaded from the MGI

http://www.informatics.jax.org/), normalized by transcript length and the two datasets (*i.e.* human and mouse) were co-normalized using quantile normalization.
mRNA sequencing data is available through ArrayExpress (http://www.ebi.ac.uk/arrayexpress) under accession E-MTAB-5039.

Xenograft sequencing analysis: SMAP

In order to effectively sort sequences based on their specie identity, we developed a process that we termed SMAP for Simultaneous Mapping for Patient-derived xenograft. The method is aligner independent and runs in three steps. First, a chimeric genome (and/or transcriptome depending on the alignment strategy) is constructed by the concatenation of the human and mouse genomes. Then, a conventional alignment pipeline processes the unsorted sequencing reads using the chimeric genome, thereby mapping all sequences simultaneously on both genomes. Finally, aligned reads are separated based on which part of the chimeric genome they were mapped, human or mouse, and all reads with an identical alignment score on both genomes are removed. The output of SMAP is a strictly distinct pair of aligned reads file (BAM), one mouse and one human. Common analysis can then be applied separately such as mutation calling, copy number analysis or gene expression quantification. SMAP was also used in association to STAR and STAR-fusion to identify and filter human chimeric transcripts.

Unsupervised and differential analysis

Single-omics clustering - Unsupervised clustering analysis was carried out on: protein coding gene expression (RNAseq, 30 samples), long non-coding gene expression (RNAseq, 30 samples), miRNA expression (miRseq, 29 samples), non-island CpG methylation (Infinium BeadChip, 30 samples) and island CpG methylation (Infinium BeadChip, 30 samples). For sequence or chip based data, an extension of the ConsensusClusterPlus algorithm was used [22]. In brief, using all paired combination of distance metrics (Euclidean, Pearson and Spearman) and linkage (Ward, complete and average), hierarchical clustering is bootstrapped in 1,000 iterations of resampling of the most variant features. An additional level of iteration adjusts the threshold of feature variability. The consensus is given by a final hierarchical clustering using the complete linkage and the number of co-classification as sample distance. For Methylation chips and SNP chips, the standard deviation was used as a measure of variability and 10 thresholds between 1% and 10% were used for each iteration of ConsensusClusterPlus. To take into account the specificity of the mean-variance relationship in count data [23], a combination of mean and standard deviation of the log-counts (minimum rank of both) was used to select between 1% and 50% of the most variable and expressed features in RNAseq.
Multi-omics clustering – The 5 non-genetic tumor omics classifications (Protein coding mRNA, long-noncoding RNA, micro-RNA, CpG-island methylation and non-CpG island methylation while excluding SNP and exome) consistently classified a majority of samples in the exact same subtypes. The tumor consensus multi-omics classification was derived

from the single-omics classification to each sample using a majority vote approach. Each sample was assigned the subtype that was given by at least 4/5 of the single-omics classification. Two samples (PDAC009T and PDAC014T) had too many divergent single-omics classifications and therefore were defined as outlier.

Differential analysis - Differential genes in RNAseq were defined using the limma-voom approach [23] and a one way ANOVA for all other types of data.

Blind source separation - Blind source separation of RNAseq-based stromal transcriptome profiles was performed using the JADE (joint approximate diagonalization of eigeinmatrices) algorithm [24] for Independent Component Analysis. Two independent components were extracted from the expression data. Genes contributing to each component were selected by thresholding the gene weights at 2 standard deviations from mean and at least 3 standard deviations from the weights in the other component.

Public dataset comparison

Three published studies were used in addition to the yet unpublished TCGA data.

TCGA –TCGA data were downloaded through the Broad Institute TCGA GDAC firehose tool (gdac.broadinstitute.org, 20160411 data snapshot).

ICGC – Methylation chips, RNAseq and microarray gene expression datasets were downloaded from the ICGC data portal (dcc.icgc.org, release 20). The subtype labels were available only for the 96 samples profiled by RNAseq all of which were also profiled using a methylome chip. The gene expression and methylation signatures for each of the four subtypes (Progenitor, Squamous, Immunogenic and ADEX) were selected from a differential analysis on the basis of a one-versus-all comparison (limma for gene expression and Student's t test for methylation). The 1,000 most differentially expressed gene or methylated CpG were used as gene/CpG signatures. Signatures are available as Supplementary table 2.

Moffitt et al. – Gene expression datasets were downloaded from the provided Gene Expression Omnibus entry GSE71729 [1]. All non-cancer samples were removed for tumor subtype analysis and before any gene-wise data centering. Gene signatures (Basal, Classical, Immune, Activated Stroma and Normal Stroma) were taken from Supplementary Table S2 of the article by Moffitt *et al*.

Collisson et al. – Gene expression datasets were downloaded from the provided Gene Expression Omnibus entry GSE17891 [25]. Subtype gene signatures are defined in the article as part of the "PDAssigner" genes as available in the supplementary table 3 of the article by Collisson et al.

Classifiers – Centroid classifiers were built for each dataset describing a classification using an approach described in previous work [26,27]. Briefly, after gene-wise centering, a centroid was built for each subtype using all the genes from the signatures. Gene expression or methylation profiles of samples to test were then correlated (Pearson's correlation) to all the centroids of a classification system (using only the subset of genes

available in both datasets) and the closest centroid class (highest correlation coefficient) was assigned. When specified, indeterminate samples correspond to samples that did not significantly correlated to any centroid (Pearson correlation test, alpha=5%).
CIT tumor and stroma classifiers – The classifiers used to predict the CIT tumor and stroma subtypes were derived in a similar manner. The first 1000 most differentially expressed human genes and mouse genes were used as signatures for the tumor and stromal subtype respectively. After gene-wise mean centering, a centroid was built using the mean expression of these genes in the sets of samples of each of the subtypes. The centroids are reported in Supplementary table 2. Given When predicting these subtypes in human primary samples, the 37 genes that were present in both centroids. Although the results were virtually identical, this was done for rational reasons as it is not possible to determinate in human primary tumors if the transcriptional signal originates from the stromal or tumor compartment, unlike in PDX.

Metabolomics
Metabolomics profiles were generated by OWL metabolomics (Derio, Spain). Metabolite extraction was accomplished by fractionating the tissue samples into pools of species with similar physicochemical properties, using appropriate combinations of organic solvents. Four different combination of extraction and UPLC-MS methods were used according to the target analytes' chemical class as previously described [28,29]. All data were processed using the TargetLynx application manager for MassLynx 4.1 software (Waters Corp., Milford, USA). A set of predefined retention time, mass-to-charge ratio pairs, Rt- m/z, corresponding to metabolites included in the analysis were used in the program. Associated extracted ion chromatograms (mass tolerance window = 0.05 Da) were then peak-detected and noise-reduced in both the LC and MS domains such that only true metabolite related features are processed by the software. A list of chromatographic peak areas was then generated for each sample injection. Normalization factors were calculated for each metabolite by dividing their intensities in each sample by the recorded intensity of an appropriate internal standard in that same sample as previously described [30].

Primary cell culture and sensitivity
Primary cell cultures were obtained from PDX. Tissues were split into several small pieces and processed in a biosafety chamber. After a fine mincing, they were treated with collagenase type V (ref C9263; Sigma) and trypsin/EDTA (ref 25200-056; Gibco, Life Technologies) and suspended in DMEM supplemented with 1% w/w Penicillin/Streptomycin (Gibco, Life Technologies) and 10% Fetal Bovine Serum (Lonza). After centrifugation, cells were re-suspended in Serum Free Ductal Media (SFDM) adapted from Schreiber et al. [31] without antibiotic and incubated at 37°C in a 5% CO_2 incubator. Cells were screened for their chemosensitivity to Ezetimibe compound (Selleck

Chemicals, Houston, TX, USA). Five thousand cells per well were plated in 96-wells plates in SFDM medium. Twenty-four hours later the media was supplemented with increasing concentrations of Ezetimibe and incubated for an additional 72 h period. Cell viability was estimated with the PrestoBlue (Invitrogen, Grand Island, NY) reagent. Each experiment was done in triplicate and repeated at least three times. Six increasing concentrations of Ezetimibe were used ranging from 0 to 100 µM.
The RNA profile of each cell culture showed a contamination in murine cells of less than 3%.

Knockdown NPC1L1 expression by siRNA transfection
Two specific siRNA directed against NPC1L1 transcript were purchased from Dharmacon (refs A-008048-13-0005 [siRNA_1] and A-008048-14-0005 [siRNA_2]) as well as a non-targeting siRNA (ref D-001910-01-05 [siRNA_cont]) and a fluorescent Green non-targeting siRNA (ref D-001950-01-05). Pancreatic PDX cells were transfected with both siRNAs against NPC1L1 following the manufacturer's protocol, cultured for 72h, and then the cell viability was measured with the PrestoBlue (Invitrogen, Grand Island, NY) reagent. Each experiment was done in triplicate and repeated two times. To investigate for efficiency of transfection, we used Accell Green non-targeting siRNA and found that transfection was over the 95% in all tested cells.

Spheroids sensitivity to Ezetimibe
Fifteen thousand cells per well were seeded in 96-well round bottom plates with medium containing 20% methylcellulose (Sigma-Aldrich, St Louis, MO, USA). After 48 h incubation, cells with spheroids of uniform size and shape were incubated with 50 µM Ezetimibe during 72h. Spheroid growth was monitored for 96h by taking microphotographies every day or assessed with the CellTiter-Glo 3D kit at the end of the treatment according to the manufacturer instructions (Promega, Madison, Wisconsin). Values were normalized and expressed as the % of the control treatment (DMSO 0.05%).

Pancreatic organoids generation and treatment with Ezetimibe
Fresh tissue samples obtained from PDX (~50 mg) were washed with resuspension medium [DMEM + 1% BSA + 1% penicillin:streptomycin]. The pieces were dissociated by mechanical cutting with scalpel blades into smaller pieces (~0.5 to 1 mm). The pulps obtained were transferred into 15 ml tubes and incubated with digestion media [DMEM + collagenase/dispase mix (1 mg/ml)] for 30 min at 37°C. Digested pulps were gently spin and supernatants were discard and replaced with 2 ml of StemPro Accutase cell dissociation reagent (Life Technology) for an additional 30 min period at 37°C. The incubation was then stopped with 1 ml resuspension media. Mixtures were filtered on cell EASY strainer 100 µm (Greiner Bio One) and resuspended into 1 ml Pancreatic Organoids Feeding Medium (POFM) [DMEM:F12 + EGF (0.05 µg/ml) + FGF (0.1 µg/ml)

+ Gastrin (1nM) + mNoggin (0.1µg/ml) + N-Acetylcystein 1.25 mM + Nicotinamide (10mM) + human R-spondin (1µg/ml) + GFR MatriGel (5%)] as previously described [32]. Organoids suspensions were then placed into 12 well plate coated with 100 µl GFR MatriGel. Media were replaced every 2-3 days. Twenty-four hours after seeding, organoids were incubated with 100 µl POFM supplemented with 50 µM Ezetimibe or 100 µl POFM supplemented with vehicle (0.5% DMSO) into 96 well plates coated with 15 µl MatriGel GFR. Organoids growth was monitored for 96h by taking microphotographies every day or assessed with the CellTiter-Glo 3D kit at the end of the treatment. Values were normalized and expressed as the % of the control.

Tissue microarray

Xenografts from PDAC samples corresponding to 29 patients were formalin-fixed. The procedure for construction of tissue microarrays (TMA) was as previously described [33,34]. Briefly, cores were punched from the selected paraffin blocks, and distributed in new blocks including two cores of 0.6-mm diameter for each tumor. To avoid false positive staining that might result from necrotic areas that could react with the antibodies tested, the tumor areas selected for the punches were dense carcinomatous. All the TMAs blocks were stored at 4°C.

Immunohistochemistry

TMA serial tissue sections were prepared 24 hours before IHC processing and stored at 4°C. The immunoperoxidase procedures were performed using an automated Ventana Benchmark XT autostainer. This device allowed identical well-controlled procedures for antigen retrieval and Ventana kits. Markers were detected using commercially available antibodies. $PPAR_{\gamma}$ (E-8) : sc-7273, (Santa Cruz Biotechnology, Inc.) 1/100; MUC17 (NBP1-91013), Novusbio, 1/100, FABP5: FABP5 (D1A7T), Cell Signaling, 1/300 and NPC1L1 (NB400-128), Nuvusbio, 1/100.

Supplementary bibliography

1. Moffitt, R. A. *et al.* Virtual microdissection identifies distinct tumor- and stroma-specific subtypes of pancreatic ductal adenocarcinoma. *Nature Genetics* **47,** 1168–1178 (2015).
2. Bailey, P. *et al.* Genomic analyses identify molecular subtypes of pancreatic cancer. *Nature* **531,** 47–52 (2016).
3. Conway, T. *et al.* Xenome--a tool for classifying reads from xenograft samples. *Bioinformatics* **28,** i172–8 (2012).
4. Banneau, G., Ayadi, P. M., Armenoult, L. & Carvalho, E. *Homogenization of cartilage tumors to extract total RNA to microarray and sequencing analysis using*

Precellys bead-beating technology. 52:196–197 (BioTechniques, 2012). doi:10.2144/000113829
5. Li, H. Aligning sequence reads, clone sequences and assembly contigs with BWA-MEM. *arXiv.org* (2013).
6. McKenna, A. *et al.* The Genome Analysis Toolkit: A MapReduce framework for analyzing next-generation DNA sequencing data. *Genome Research* **20,** 1297–1303 (2010).
7. Van der Auwera, G. A. *et al.* From FastQ data to high confidence variant calls: the Genome Analysis Toolkit best practices pipeline. *Curr Protoc Bioinformatics* **43,** 11.10.1–33 (2013).
8. Cibulskis, K. *et al.* Sensitive detection of somatic point mutations in impure and heterogeneous cancer samples. *Nature Biotechnology* **31,** 213–219 (2013).
9. Wang, K., Li, M. & Hakonarson, H. ANNOVAR: functional annotation of genetic variants from high-throughput sequencing data. *Nucleic Acids Res.* **38,** e164–e164 (2010).
10. Staaf, J. *et al.* Normalization of Illumina Infinium whole-genome SNP data improves copy number estimates and allelic intensity ratios. *BMC Bioinformatics* **9,** 409 (2008).
11. Venkatraman, E. S. & Olshen, A. B. A faster circular binary segmentation algorithm for the analysis of array CGH data. *Bioinformatics* **23,** 657–663 (2007).
12. Popova, T. *et al.* Genome Alteration Print (GAP): a tool to visualize and mine complex cancer genomic profiles obtained by SNP arrays. *Genome Biol* **10,** R128 (2009).
13. Toyota, M. *et al.* CpG island methylator phenotype in colorectal cancer. *Proc. Natl. Acad. Sci. U.S.A.* **96,** 8681–8686 (1999).
14. Nones, K. *et al.* Genome-wide DNA methylation patterns in pancreatic ductal adenocarcinoma reveal epigenetic deregulation of SLIT-ROBO, ITGA2 and MET signaling. *Int. J. Cancer* **135,** 1110–1118 (2014).
15. Vigneault, F. *et al.* High-throughput multiplex sequencing of miRNA. *Curr Protoc Hum Genet* **Chapter 11,** Unit 11.12.1–10 (2012).
16. Barturen, G. *et al.* sRNAbench: profiling of small RNAs and its sequence variants in single or multi-species high-throughput experiments. *Methods in Next Generation Sequencing* **1,**
17. Bullard, J. H., Purdom, E., Hansen, K. D. & Dudoit, S. Evaluation of statistical methods for normalization and differential expression in mRNA-Seq experiments. *BMC Bioinformatics* **11,** 94 (2010).
18. Dobin, A. *et al.* STAR: ultrafast universal RNA-seq aligner. *Bioinformatics* **29,** 15–21 (2013).
19. Liao, Y., Smyth, G. K. & Shi, W. featureCounts: an efficient general purpose program for assigning sequence reads to genomic features. *Bioinformatics* **30,** 923–930 (2014).
20. Carlevaro-Fita, J., Rahim, A., Guigó, R., Vardy, L. A. & Johnson, R. Cytoplasmic long noncoding RNAs are frequently bound to and degraded at ribosomes in human cells. *RNA* **22,** 867–882 (2016).
21. Becht, E. *et al.* Immune and Stromal Classification of Colorectal Cancer Is Associated with Molecular Subtypes and Relevant for Precision Immunotherapy.

Clinical Cancer Research **22,** 4057–4066 (2016).
22. Wilkerson, M. D. & Hayes, D. N. ConsensusClusterPlus: a class discovery tool with confidence assessments and item tracking. *Bioinformatics* **26,** 1572–1573 (2010).
23. Law, C. W., Chen, Y., Shi, W. & Smyth, G. K. voom: Precision weights unlock linear model analysis tools for RNA-seq read counts. *Genome Biol* **15,** R29 (2014).
24. Cardoso, J. F. & Souloumiac, A. Blind beamforming for non-Gaussian signals. *IEE Proceedings F - Radar and Signal Processing* **140,** 362–370 (1993).
25. Collisson, E. A. *et al.* Subtypes of pancreatic ductal adenocarcinoma and their differing responses to therapy. *Nature Medicine* **17,** 500–503 (2011).
26. Marisa, L. *et al.* Gene expression classification of colon cancer into molecular subtypes: characterization, validation, and prognostic value. *PLoS Med.* **10,** e1001453 (2013).
27. Guinney, J. *et al.* The consensus molecular subtypes of colorectal cancer. *Nature Medicine* **21,** 1350–1356 (2015).
28. Barr, J. *et al.* Liquid chromatography-mass spectrometry-based parallel metabolic profiling of human and mouse model serum reveals putative biomarkers associated with the progression of nonalcoholic fatty liver disease. *J. Proteome Res.* **9,** 4501–4512 (2010).
29. Barr, J. *et al.* Obesity-dependent metabolic signatures associated with nonalcoholic fatty liver disease progression. *J. Proteome Res.* **11,** 2521–2532 (2012).
30. Martínez-Arranz, I. *et al.* Enhancing metabolomics research through data mining. *J Proteomics* **127,** 275–288 (2015).
31. Schreiber, F. S. *et al.* Successful growth and characterization of mouse pancreatic ductal cells: functional properties of the Ki-RASG12V oncogene. *Gastroenterology* **127,** 250–260 (2004).
32. Huang, L. *et al.* Ductal pancreatic cancer modeling and drug screening using human pluripotent stem cell- and patient-derived tumor organoids. *Nature Medicine* **21,** 1364–1371 (2015).
33. Giusiano, S. *et al.* Immunohistochemical profiling of node negative breast carcinomas allows prediction of metastatic risk. *Int. J. Oncol.* **36,** 889–898 (2010).
34. Charpin, C. *et al.* Validation of an immunohistochemical signature predictive of 8-year outcome for patients with breast carcinoma. *Int. J. Cancer* **131,** E236–43 (2012).